Nanoscale Advances

ROYAL SOCIETY OF CHEMISTRY

REVIEW

View Article Online
View Journal | View Issue

Cite this: *Nanoscale Adv.*, 2021, **3**, 6514

Recent trends in gas sensing *via* carbon nanomaterials: outlook and challenges

Pallvi Dariyal,[ab] Sushant Sharma,[bc] Gaurav Singh Chauhan,[ab] Bhanu Pratap Singh *[ab] and Sanjay R. Dhakate *[ab]

The presence of harmful and poisonous gases in the environment can have dangerous effects on human health, and therefore portable, flexible, and highly sensitive gas sensors are in high demand for environmental monitoring, pollution control, and medical diagnosis. Currently, the commercialized sensors are based on metal oxides, which generally operate at high temperatures. Additionally, the desorption of chemisorbed gas molecules is also challenging. Hence, due to the large surface area, high flexibility, and good electrical properties of carbon nanomaterials (CNMs) such as carbon nanotubes, graphene and their derivatives (graphene oxide, reduced graphene oxide, and graphene quantum dots), they are considered to be the most promising chemiresistive sensing materials, where their electrical resistance is affected by their interaction with the analyte. Further, to increase their selectivity, nanocomposites of CNMs with metal oxides, metallic nanoparticles, chalcogenides, and polymers have been studied, which exhibit better sensing capabilities even at room temperature. This review summarizes the state-of-the-art progress in research related to CNMs-based sensors. Moreover, to better understand the analyte adsorption on the surface of CNMs, various sensing mechanisms and dependent sensing parameters are discussed. Further, several existing challenges related to CNMs-based gas sensors are elucidated herein, which can pave the way for future research in this area.

Received 23rd September 2021
Accepted 1st October 2021

DOI: 10.1039/d1na00707f

rsc.li/nanoscale-advances

1. Introduction

The modern living standard is critically affecting the environment due to the continuous production of toxic gases, where their invisibility is a serious concern. Air pollutants such as NO_2, CO_x, and CH_4 are the major reason for the dangerous atmospheric changes, which are part of the environmental changes resulting in an increase in the Earth's temperature. Together with pollutant gases, there are several other hazardous gases in the surroundings such as CH_4, NH_3, H_2, and H_2S, which become explosive when mixed with air in a certain proportion. Besides these toxic gases, the vapours of numerous volatile organic compounds (VOCs) such as ethanol, toluene, triethylamine (TEA), formaldehyde, and acetone are another class of harmful gases that is dangerous to human health. Hence, it is essential to sense these gases for environmental analysis, industrial emission monitoring, medical diagnosis, agriculture, public safety and security purposes. Therefore, there is a strong demand for highly sensitive, portable, flexible, and cost-effective gas sensors. Depending on their sensing mechanism, there are various types of sensors, *i.e.*, chemiresistive,[1] field-effect transistor (FET),[2] and microelectromechanical system (MEMS)[3] gas sensors, where chemiresistive sensors are highly explored.

Currently, metal-oxide sensors (MOSs) are well commercialized for various practical applications such as hand-held ethanol sensors for drunk and driving cases, methane and hydrogen sensors for the safety of labours working in industries and mines, and acetone and toluene gas sensors for diabetic and lung cancer diagnosis.[4] Thus far, SnO_2, TiO_2, WO_3, ZnO, CuO, CdO and In_2O_3 have been widely considered for these real-life sensing applications. However, although these sensors show high sensitivity, their operating temperatures are fairly high, which increase their operational and maintenance cost. Furthermore, their sensitivity is affected by a change in their surface morphology. For instance, a hollow sphere (3-D) WO_3-based sensor[5] exhibited a higher sensing response than a 2-D thin film[6] for the detection of 1 ppm NO_2. Additionally, the recovery time is very high for these sensors given that the analytes are chemisorbed with a high binding energy. Although many phenomena, *i.e.*, thermal treatment[7] and UV irradiation,[8] have been employed for chemical desorption, the recovery time is still very long.

Therefore, to overcome the aforementioned issues, new alternatives, *i.e.*, carbon nanomaterials (CNMs), have been explored as sensing materials in the past two decades.[9–12] These

[a]*Advanced Carbon Products and Metrology, CSIR-National Physical Laboratory, Dr K. S. Krishnan Marg, New Delhi, 110012, India. E-mail: bps@nplindia.org; dhakate@nplindia.org*

[b]*Academy of Scientific and Innovative Research (AcSIR), Ghaziabad-201002, India*

[c]*University of Ulsan, Chemical Engineering Department, Ulsan, 44610, South Korea*

CNMs offer a high surface area for absorption, which enables them to achieve high sensitivity. CNMs, *i.e.* CNTs, graphene, and their derivatives, possess high electron transportation properties with low noise. Moreover, CNMs gas sensors enable fast recovery *via* UV light. Additionally, their robustness is suitable for developing portable and flexible devices with high sensitivity to cost ratio. Thus, CNMs-based gas sensors are widely used in various fields, as shown in Fig. 1. The most recent application is to predict physiological conditions in the human body by detecting several VOCs exhaled during breathing.[13–15]

Despite the numerous advantages of pristine CNMs, they also have some serious drawbacks, such as low selectivity, low repeatability, and non-uniformity of the functional groups on graphene derivatives or number of CNT walls.[16,17] Hence, without sacrificing their advantages, nanocomposites of CNMs with metal oxides, metallic nanoparticles, chalcogenides, and polymers, have been studied, and this new class of CNMs hybrid sensing materials has shown tremendous performances. Moreover, CNMs have good flexibility,[18–20] and therefore can be employed to fabricate wearable sensors.

Numerous reviews have reported the recent progress on CNTs and graphene sensors. Recently, Sireesha *et al.* reported a broad review on CNT-based biosensors.[21] Furthermore, Seesaard *et al.* described metal oxide-decorated or doped CNT-based hybrid nanocomposites as future sensors.[22] In a similar direction, the current progress on CNT-based flexible sensors for CO_2, H_2S and NH_3 was reviewed by Kumar.[23] Another CNM (graphene) has also been explored and numerous articles have been published in the last decade (shown as the outer circle in Fig. 2). In 2018, Tian *et al.* proposed pristine, defected and functionalized graphene-based sensors.[24] Further, a thorough review on graphene oxide as NO_2, H_2, NH_3, H_2S, acetone and humidity sensors was presented by Toda.[12] Similarly, Martínez *et al.* presented a theoretical overview on graphene-based sensors for toxic gases.[25] However, there are numerous reviews published on CNTs and graphene-based gas sensors individually, only a few reviews summarized both CNMs (CNTs and graphene)-based chemiresistive sensors in a comparative manner.[10,26–28] Therefore, it is important to identify new trends in this area. The latest research on these two CNMs and their mechanism are explained briefly in this review. This review contains prominent parameters of CNMs as sensing materials. The significant research works on CNMs chemiresistive sensors towards various gases (greenhouse, explosive, and VOCs) are covered in this review. Moreover, the significant works done on CNM-based nanocomposites as gas sensors and their possible sensing mechanisms are also emphasized. Additionally, the selectivity and sensitivity enhancement factors of various dopants for CNMs and the responsible mechanisms are elaborated. Briefly, the latest achievements on CNMs in the sensing domain are discussed and their outlook for futuristic technologies is highlighted.

2. Properties of carbon nanostructures for air-quality sensing

Carbon nanostructures such as CNTs and graphene have many distinct properties, which have been exploited to develop next-generation sensors.[29] The morphology, surface area, conductivity, chemical activity, and desorption ability of sensing materials are essential aspects for chemiresistive gas sensors, which are described in detail below.

2.1 Morphology of sensing material

The efficiency of a sensor is highly influenced by its morphology.[30] There are various morphologies of sensing materials, which can be classified as zero-dimensional

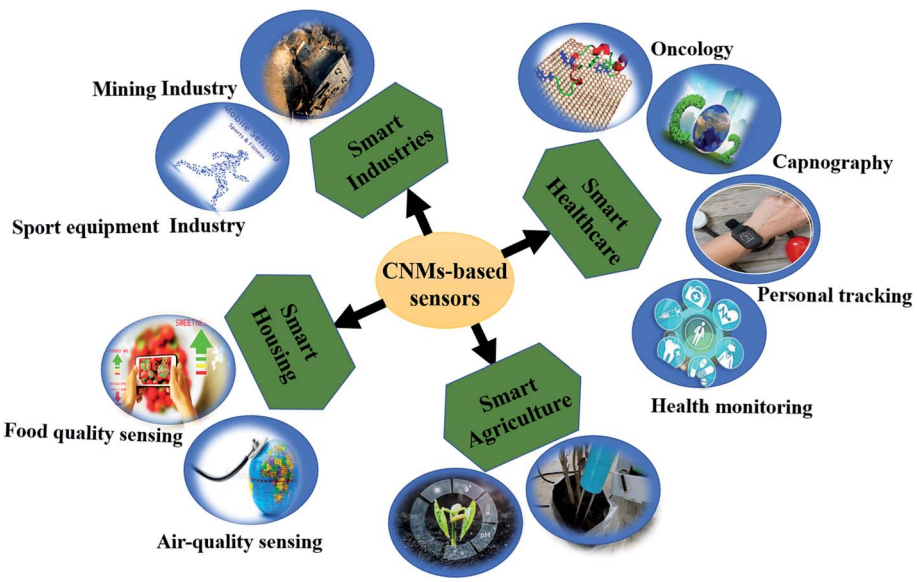

Fig. 1 Application of CNMs-based sensors in various fields.

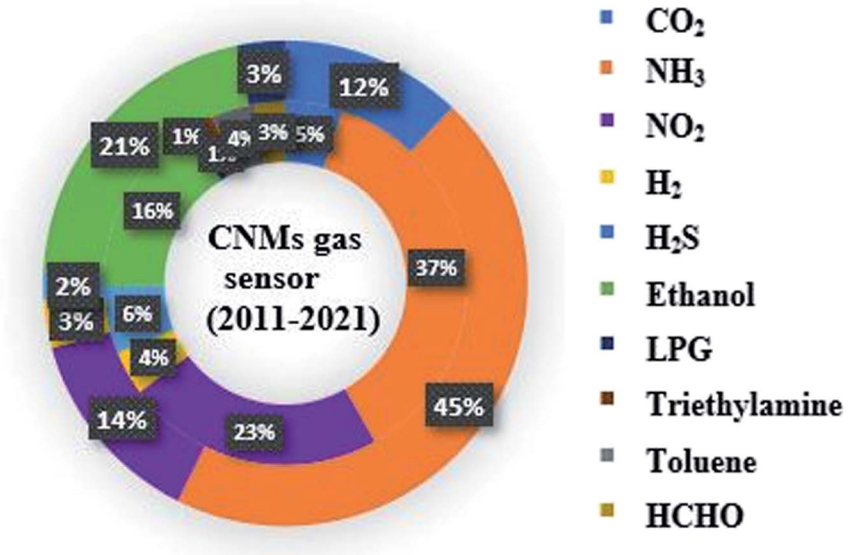

Fig. 2 Concentric pie chart representing the number of publications on CNT- (inner circle) and graphene (outer circle)-based gas/vapor sensors for the period 2011 to 2021 (data obtained on May, 2021, from Scopus).

(quantum dots),[31,32] one-dimensional (nanowires and nanotubes),[33,34] two-dimensional (sheets and belts),[35] and three-dimensional (composed of 0-D, 1-D, and 2-D structures).[36,37] These different morphologies have different advantages, including abundant surface active sites, high sensing rate, and enhanced gas diffusion. Among them, 3-D structures have the highest number of active sites, but their synthesis is complex. Therefore, the most preferred structures for high sensing performances are hollow 1-D and porous 2-D nanostructures given that they possess a large surface area for the adsorption of target gases. Accordingly, 1-D CNTs and 2-D graphene sheets are considered ideal sensing materials. In CNTs, their inner and outer surface can act as adsorption sites, while in graphene sheets, analytes can adsorb on their surface and penetrate their porous sheets (as shown in Fig. 3).

2.2 High surface area and absorption capacity

For the adsorption of atmospheric oxygen and gas molecules, adsorption sites should be available. Therefore, a high surface area possessing abundant adsorption sites is essential. Graphene and CNTs both have a high surface area, which depends on their synthetic conditions, post-treatment, and available functional groups on their surface. The specific surface area of various CNMs, including graphene and its derivatives, CNTs, and CNFs, is presented in Table 1.

As mentioned in Table 1, CNFs have a very low specific surface area. Therefore, they have been explored the least as a gas sensing material. On the contrary, although graphene quantum dots (GrQDs) also have a low specific surface area, they have high charge mobility (due to quantum effects) and low toxicity.[55] Therefore, nowadays, researchers are focusing on GrQD-based biosensors. Nevertheless, the other carbon allotropes such as CNTs and graphene have a high surface area, which makes them superior sensing materials.

Graphene has almost twice the surface area of CNTs as gas analytes can adsorb on both sides of the graphene sheets, but in CNTs, together with the surface of the nanotube walls, the interior pore of individual tubes, grooves, and interstitial channels formed between three adjacent tubes within the bundle can also act as adsorption sites given that they are generally found in bundles.[11,56] The adsorption of analytes in these sites depends on the binding energy of the gas molecules.

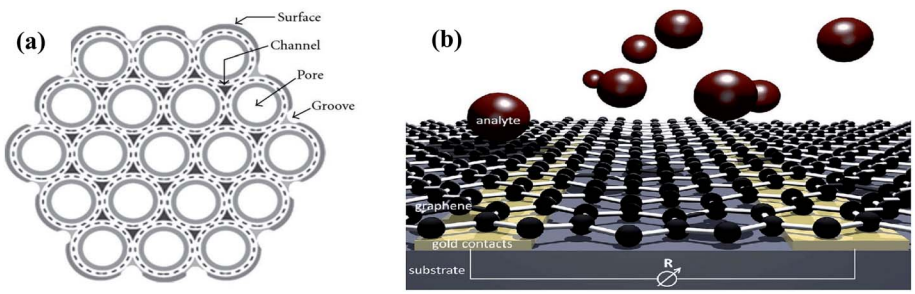

Fig. 3 Available surface area on (a) CNTs[11] (reprinted with permission from ref. 11. Copyright (2009), Hindawi Publisher, under Creative Commons Attribution 3.0 License) and (b) graphene[38] (reprinted with permission from ref. 38. Copyright (2014), The Royal Society of Chemistry).

Table 1 Specific surface area of 0-D, 1-D, 2-D, and 3-D CNMs structures

CNM structure	Sensing material	Specific surface area ($m^2\ g^{-1}$)
0-D	Graphene QDs	0.066–2.57 (ref. 31)
1-D	MWCNTs	435 (ref. 39)
	SWCNTs	600 (ref. 40)
	MWCNTs	91.223 (ref. 41)
	CNFs	14.8 (ref. 42)
	Fluorinated CNFs having carbon black	21 (ref. 43)
2-D	Monolayer graphene	2630 (ref. 44)
	Nanoporous graphene	410.99 (ref. 45)
	Laser-induced graphene	350 (ref. 46)
	Monolayer GO	2391 (ref. 47)
	GO sheet	37.24 (ref. 48)
	GOQDs	324 (ref. 49)
	rGO	64 (ref. 50)
	Superhydrophobic rGO	850 (ref. 37)
	N doped rGO	335.6 (ref. 51)
	N doped rGO	247.7 (ref. 52)
3-D	1-D MWCNT + 2-D Gr (50%)	151.3 (ref. 53)
	WS_2-1-D CNFs	6.44 (ref. 54)

Additionally, these sites may not adsorb certain gases if the dimensions of the gas molecules are larger than the diameter of the site.

2.3. Electrical conductivity

For chemiresistive sensors, their responses are evaluated in terms of change in resistance. In zero bandgap graphene, the mobility of electrons is very high, which makes it easier to respond to gases. For the adsorption of gas molecules in 2-D graphene, the adsorption energy can be calculated using eqn (1).

$$E_a = E_{(\text{sensing material+gas})} - E_{(\text{sensing material})} + E_{(\text{gas})} \quad (1)$$

where $E_{(\text{sensing material+gas})}$, $E_{(\text{sensing material})}$ and $E_{(\text{gas})}$ represent the total energy of the system formed by the sensing material and the analyte gas, energy of 2-D graphene and energy of analyte gas, respectively.

Moreover, the bandgap of semiconducting CNTs can tuned *via* easy electron transfer phenomena. Furthermore, the oxygen groups of graphene derivatives, transition metal catalyst of CNTs, and their defective sites affect their bandgap, making them sensitive towards specific gases.

2.4 Chemical activity

The intrinsic or pristine sensing materials show less interaction with analyte molecules due to the lack of defects or reactive sites on their surface.[57] The presence of functional groups promotes gas adsorption.[58] Moreover, these functional groups also help to improve the selectivity. Due to these favorable features, high chemical activity is crucial for improved sensing efficiencies, which contributes to the generation of more reactive sites (shown in Fig. 4). Both, CNTs and graphene have highly reactive surfaces, which are created by refluxing them.

In terms of graphene derivatives, GO and rGO are preferable in comparison to pure graphene due to the presence of oxygen functional groups. Moreover, functionalized CNTs show a higher response than pristine CNTs,[57,59] but their surface area depends on the refluxing process, *i.e.* time, temperature, and acid used.[60] Due to this property, hybrid CNMs composites are easy to synthesize, which are the most recent researched sensing material.

2.5 Desorption of analyte

For long-term usability, the most important feature of sensors is the desorption of gas molecules with a fast recovery rate. In MOS sensors, thermal energy is essential for the desorption of gas molecules. Therefore, an in-built micro-heater should be present in the device, which makes it expensive and complex to design.[7] Besides, it may also decrease the working life of sensors. Therefore, it is a challenge to recover the baseline resistance in MOS sensors within seconds at room temperature.

However, in CNMs-based sensors, the recovery is accelerated with external energy, which can desorb the molecules attached to their surfaces. Accordingly, light activation is a tremendous technique, which contributes to reduce power consumption and miniaturization of sensing devices. Generally, UV and IR light are used for faster recovery in CNMs. UV light removes the

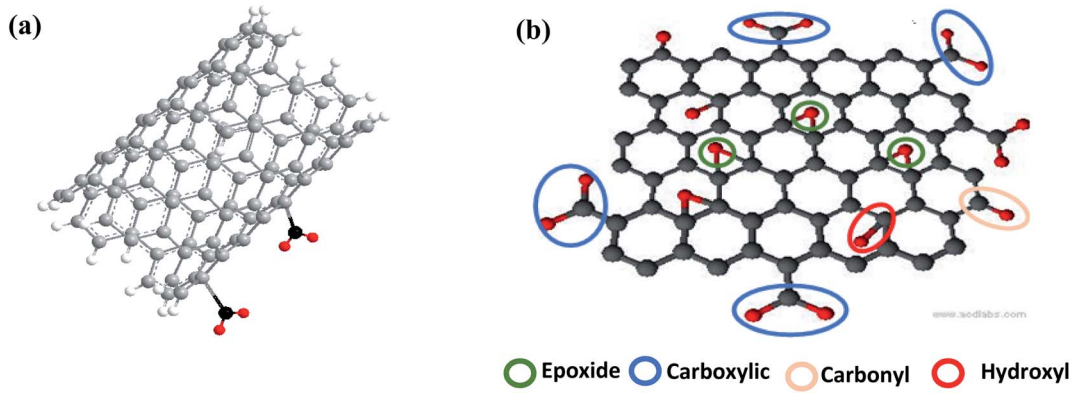

Fig. 4 Various functional groups attached on (a) CNTs and (b) graphene.

oxygen atoms attached to the surface, and hence rapidly balances the baseline resistance of CNMs-based sensors. This happens due to the surface plasmon resonance occurring in the graphene layers or CNTs at very high frequency. The as-generated vibrations cause the analyte and oxygen to leave the CNMs surface. Conversely, IR light generates electron–hole (E–H) pairs in graphene, and when these E–H pairs recombine, photon radiation occurs. This radiation heat recovers the resistance of CNT. The other advantage of the light activation technique is its higher sensitivity given that UV light can affect the electronic properties by increasing the concentration of photocarriers, improving the interaction between the analyte molecules and sensing material.[8] Hence, this technique is very beneficial for high sensitivity, stability, portability, and low power consumption in ideal chemiresistive gas sensors. Furthermore, in hybrid CNM sensing materials, besides UV light, visible, IR, and white light are also studied for the desorption of gas molecules.[61,62]

3. CNMs as gas sensing materials

Carbon nanostructures such as CNTs and graphene can detect very low concentrations of greenhouse and explosive gases. Therefore, employing the gas sensitivity of graphene and CNTs to build highly sensitive, low power-consuming gas sensors is not only of academic interest but also of great commercial interest.

3.1 CNTs as gas sensors

CNT-based gas sensors have been the topic of research given that they are easy to synthesize, compact, and inexpensive. Furthermore, the high surface area, hollow geometry, and chemical activeness of carbon nanotubes (CNTs) make them attractive for gas sensing applications. Considering that the electronic properties of CNTs are highly sensitive towards any change in their chemical environment, several exciting works on pristine CNTs as chemiresistive sensors have been widely explored, where their sensitivity is affected by the number of walls, *i.e.*, SWCNT-based sensors have higher sensitivity than MWCNTs for NO_2 sensing even at a low operating temperature. In this case, Naje *et al.* (2016) investigated SWCNTs and MWCNTs for sensing 3% NO_2 gas and observed 79.81% and 59.61% sensitivity, respectively.[63]

Due to the lower sensitivity of pristine CNTs, functionalized CNTs have also been studied to enhance the selectivity towards specific analytes. In addition, various metallic nanoparticles and metal oxides have been incorporated into CNTs to achieve specificity to different analytes. In this case, ZnO-doped SWCNTs[64] and ZnO-doped MWCNTs[65] were investigated for NO_2 sensing, which exhibited the highest sensitivity at an operating temperature of 150 °C and 300 °C, respectively. Nevertheless, the alignment of CNTs in the CNT network also affects the response of the sensor. Kumar *et al.* revealed that the highly aligned SWCNT network has seven times higher response than the randomly aligned SWCNT network towards 0.5 ppm NO_2 gas molecules.[66] Furthermore, alignment not only affects the sensitivity but also the detection limit, which can be reduced with an increase in alignment.

3.1.1 Sensing mechanism of CNTs. In CNT-based chemiresistive sensors, physisorption, chemisorption or both can occur on the surface of CNTs. In physisorption, either van der Waals forces or dipole interaction (London force) is responsible for adsorption, where no alteration of the CNT surface happens.[67–69] During sensing, energy changes due to the charge transportation or delocalization of electrons in the band diagram and the change in resistance with respect to exposed gas are measured as the response of the sensor, which depend on the type of gas analyte, its concentration and operating temperature.

When CNTs come in contact with air, ionized oxygen is adsorbed on their surface. The accumulation of oxygen ions leads to an electron depletion region (EDR), and consequently the CNTs become p-type. The change in resistance of CNTs is due to the charge transfer between the analyte and CNT surface. This interaction mechanism can be classified as oxidation and reduction,[70,71] *i.e.*, when the CNT interacts with electron-withdrawing or reducing gas/chemical (such as NH_3), the resistance of the CNT increases due to electron transfer from the gas to the CNT. Consequently, the potential barrier energy decreases. On the contrary, when electron-accepting or oxidizing gas/chemical molecules (for example NO_2) interact with the CNT surface, the gas molecules withdraw electrons from the CNTs. This increases the hole population, which decreases the resistance of the CNTs, increasing the barrier energy. Together with physisorption, chemisorption phenomena can also occur in CNTs.

Although the occurrence physisorption leads to low selectivity and sensitivity, low operating temperature, short response time, and fast recovery are advantages of physisorption, which are essential for an ideal sensor (not applied on well-commercialized MOS gas sensor). Therefore, several hazardous air pollutants such as NO_2, CO, CO_2, and CH_4, explosive gases, and VOCs have been detected *via* CNT-based gas sensors with a shorter recovery time in comparison with MOS sensors.[72] The effects of these gaseous agents have also been studied theoretically by using first-principal approximations and density calculations. In this case, Kumar *et al.* studied the adsorption mechanism theoretically *via* DFT implemented in the computational quantum chemical HF code of the 6-31G basis set on (1,1) and (2,2) CNTs.[73] They concluded that after gas exposure there is less variation in the binding energy of (1,1) CNTs (7.92%) than (2,2) CNTs (17.32%), which indicates the lower sensitivity of (1,1) CNTs. Moreover, the band gap width of (2,2) CNTs decreased because a large number of electrons is free to move, which is directly related to the higher conductivity of (2,2) CNTs.

3.2 Graphene and its derivatives as gas sensors

Besides CNTs, a lot of research on graphene-based gas sensors has been performed. Due to the availability of a large surface area for the adsorption of gas molecules, graphene and its derivatives such as graphene oxide (GO), reduced graphene

oxide (rGO), and graphene quantum dots (GrQDs) have been explored for the detection of various hazardous gases such as NO_2, H_2S, NH_3, NO_2, CO_2, CH_4 and CO gases.

3.2.1 Sensing mechanism of graphene. As previously mentioned, CNTs have a great potential for sensing applications. However, graphene shows higher sensitivity towards gases and vapors given that it has abundant adsorption sites and high charge mobility.[74] Considering that graphene also behaves like a p-type semiconductor after the chemisorption of atmospheric oxygen, its sensing mechanism is similar to that of CNTs for oxidizing and reducing gasses (described in Section 3.1.1). Furthermore, graphene is mostly preferred for flexible sensors as it has higher elasticity.[20]

Due to the properties of graphene (as mentioned in Table 2), it can act as an advanced sensing material and even show a higher response than MWCNT-based sensors given that CNTs have a lower specific surface area than graphene. Moreover, its sensitivity depends on the number of graphene layers. In this case, Seekaew *et al.* examined the effect of the number of graphene layers for sensing NO_2 and reported that bilayer graphene showed the highest response in comparison to monolayer and multi-layer graphene.[76] Except for single-layer graphene, the parabolic-shaped bands of graphene have finite charge carriers (increase with an increase in the number of layers), resulting in a reduction in resistance. Conversely, for single-layer graphene (conical-shaped bands), the concentration of electrons transferred to NO_2 gas molecules may be limited due to the lower availability of electronic states in the valence band (VB) compared with bilayer and multilayer graphene (as shown in Fig. 5a).

Fig. 5b shows the gas response of monolayer, bilayer, 3-layered, and 4-layered graphene at different concentrations (0–25 ppm) of NO_2. Additionally, the selectivity towards NO_2 was also confirmed by testing them with various gases (as shown in Fig. 5c).

Although graphene has high sensitivity, intrinsically it has low selectivity. Therefore, several non-metals such as fluorine, boron, and nitrogen have also been investigated for improving the sensing performance of graphene. In 2015, Park *et al.* investigated the sensing of NH_3 using fluorinated graphene oxide (F-GO),[77] where the presence of fluorine (high electronegativity) lowered the Fermi energy level given that electrons migrated from the valence band to the LUMO. Thus, due to the electron migration, the sensitivity was enhanced. On the

Table 2 Comparison of the properties of graphene and carbon nanotubes[42,75]

Property	Graphene	Carbon nanotubes
Elastic limit	20%	16%
Specific surface area	2360 $m^2 g^{-1}$	387 $m^2 g^{-1}$
Electrical conductivity	10^6 to 10^7 S m^{-1}	10^8 S m^{-1}
Charge mobility	200 000 $cm^2 V^{-1} s^{-1}$	80 000 $cm^2 V^{-1} s^{-1}$

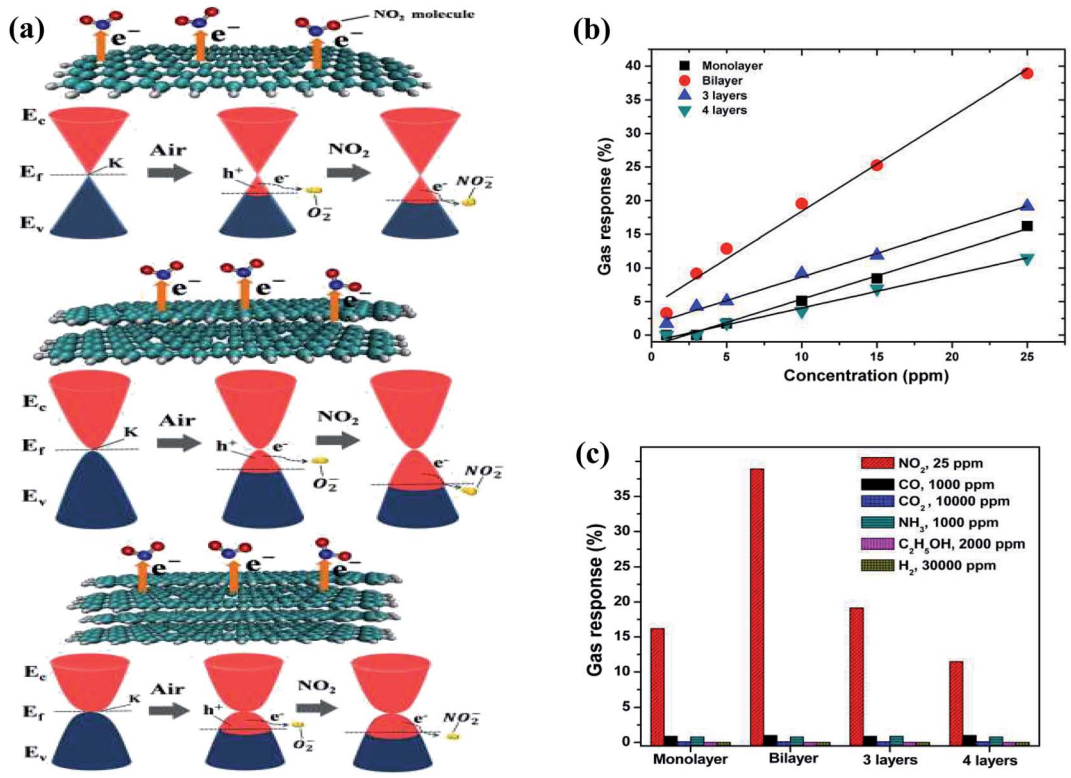

Fig. 5 (a) Schematic and band diagrams of NO_2 sensing mechanism of monolayer, bilayer and multilayer graphene gas sensors. (b) Gas response ($\Delta R/R$) of layered graphene gas sensors as a function of NO_2 concentration. (c) Selectivity plot of layered graphene-based sensor to various gases at room temperature[76] (reprinted from ref. 76, Copyright (2017), with permission from Elsevier).

contrary, the sensing material having a high fluorine to carbon ratio decreased the response of the sensor because when NH_3 gets adsorbed on F-GO, the electrons transfer to the LUMO owing to the enhanced Fermi level. Recently Srivastva *et al.* doped boron and nitrogen in a flexible graphene layer (FGL) for the detection of NH_3.[78] To achieve the strong adsorption of analyte molecules, the adsorption energy should be low. Thus, by doping boron in FGL, the adsorption energy (E_{ads}) for NH_3 decreased by two times ($E_{ads} = -0.5$ eV), which directly affected the response of the sensor.

Furthermore, functionalized graphene (GO and rGO) has also been employed for sensing applications. Recently, Gao *et al.* (2020) studied the adsorption of H_2S and CH_4 on intrinsic, defected and doped graphene theoretically using the first-principals method.[79] The required adsorption energies of intrinsic graphene, Ni-doped graphene, vacancy-defected graphene and graphene oxide for H_2S are −0.038, −0.699, −2.934 and −1.258 eV, respectively. Conversely, the required adsorption energy towards CH_4 increased in the order of intrinsic graphene (−0.022 eV), graphene oxide (−0.047 eV), Ni-doped graphene (−0.099 eV) and vacancy defeated graphene (−0.164 eV), which confirmed that intrinsic graphene requires a high E_{ads} for H_2S and CH_4, resulting in weak physisorption. Among the three modified graphene, the vacancy-defected graphene is the best candidate for the adsorption of H_2S and CH_4. Hence, controlled defects in graphene have been widely studied for gas sensing applications.[80] Furthermore, besides non-metals, various metallic particle- and metal oxide-doped graphene and their derivatives are also considered as good alternatives.[81–85]

3.3. CNM hybrid nanocomposite-based gas sensors

3.3.1 Sensing mechanism of CNM hybrid nanocomposites. As mentioned in the previous section, CNM hybrid nanocomposites composed of metal oxides (MOs), metallic nanoparticles (MNPs) and polymers are the new era of gas sensors. For CNM hybrid nanocomposites, MOs are the most explored. When MOs are introduced in CNMs, heterojunctions (p–p or p–n) are formed between the CNMs and MO junction given that they have different Fermi levels (E_F) and electrons are transported from the higher E_F to lower E_F, thus increasing the performance of the sensor.[86] Besides MOs, MNPs are also used for improving the sensing performance of CNMs. When metal nanoparticles are incorporated in CNMs, a Schottky barrier formed, given that MNPs and CNMs have different work functions (WF).[87] Simultaneously, these MNPs can also act as an electron acceptor and catalyst, which can facilitate redox reactions due to the spill-over effect. Accordingly, the response towards analytes increases compared to pristine CNMs. Furthermore, CNMs with polymers are a new choice as flexible sensors for the fabrication of bendable electronic devices.[18,88,89] Therefore, various polymers have been explored such as polyethylene terephthalate (PET), polypyrrole, polytetrafluoroethylene (PTFE), and polyaniline (PANI) as flexible substrates or CNM-doped sensing material for devices. The sensing mechanism is complex and different with different polymers, *i.e.*, when a reducing gas such as NH_3 interacts with the reactive sites of the emeraldine base of PANI, protonation/deprotonation of PANI occurs and NH^{4+} ions are formed owing to the delocalization of electrons and increase in the electronegativity on its surface.[90]

4. CNM hybrid nanocomposite-based gas sensors

4.1 NO_x sensors

Nitrogen dioxide (toxic air-pollutant) is a by-product from the burning of gasoline, fuel, *etc.* in the exhaust of vehicles. According to the Immediately Dangerous to Life and Health (IDLH) values, more than 20 ppm of NO_2 is fatal, given that this gas accelerates the risk of respiratory diseases in children and senior citizens.[91] Furthermore, in daylight, NO_x reacts with various VOCs and forms ozone, which can have several harmful effects on humans such as destruction to lung tissues and terrible effects on their functioning, mostly in asthmatic patients. Moreover, NO_x gases can cause other environmental problems such as smog and acid rain. Due to the above-mentioned serious environmental threats, several governments have established many laws to limit NO_x emissions. Therefore, the detection of NO_x is necessary to employ some sort of feedback loop in the combustion process for its minimization.

4.1.1 Sensing with CNTs and their hybrid nanocomposites. To understand the interaction between CNTs and NO_2, theoretical studies on NO_2 sensing on the surface of SWCNTs and metal-doped SWCNTs *via* first-principal approximations were performed, where the analysis of electron density showed the mechanism of charge transfer induced from the CNTs to NO_2 molecules.[92] The calculated bandgap of pristine SWCNTs, Cu, Pt, and Ti-doped (8,0) SWCNTs is 0.63, 0.197, 0.376 and 0.504 eV, respectively, which confirms the higher stability and lower conductivity of pristine CNTs and Ti-doped CNTs. However, Ti-doped SWCNTs showed the highest charge transfer (0.456 eV), and thus the highest sensitivity compared with Pt (0.385 eV) and Cu (0.351 eV)-doped CNT.

Furthermore, numerous experimental studies have been performed on CNT-based NO_2 sensors. One of the pioneering works involved the detection of NO_2 on MoS_2 (chalcogenide)-decorated vertically aligned CNTs (VACNTs) grown on an Si substrate.[34] When the as-designed sensor was exposed to an NO_2 gas atmosphere, NO_2 molecules were adsorbed on the edges and surface of the MoS_2 hexagonal-shaped nanoplates (HNPs), where the electronic charge transferred from MoS_2 to the gas molecules (illustrated in Fig. 6a), consequently decreasing the resistance of the sensor. In addition, NO_2 gas molecules also adsorbed on the surface of the CNTs, which decreased the overall resistance of the sensor.

The as-made sensor showed a sensitivity of 0.023% × ppb (shown in Fig. 6b).

Further, Su *et al.* detected NO_2 gas on Au and Ag-decorated WO_3-functionalized MWCNTs.[8] Besides WO_3 and CNTs, the gas molecules were also adsorbed on Au and Ag and due to

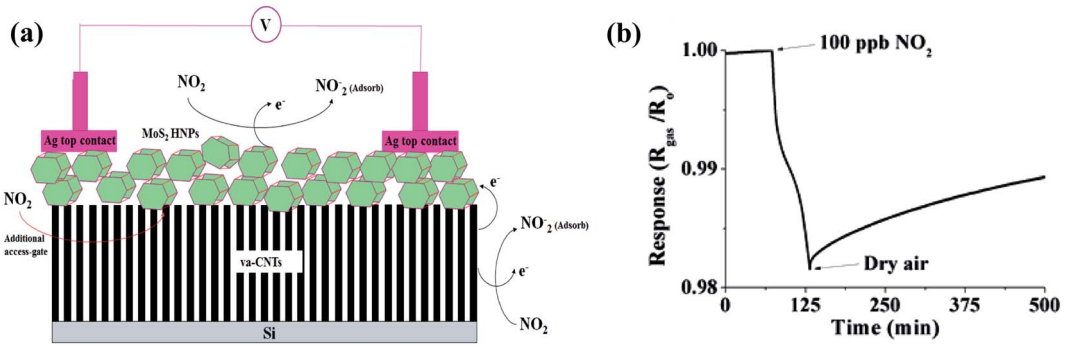

Fig. 6 (a) Schematic explaining the sensing mechanism of MoS_2 hexagonal nanoparticles (HNPs) on vertically aligned CNT array-based sensor. (b) Response of sensor at 100 ppb NO_2 gas[34] (reprinted with permission from ref. 34. Copyright (2017), John Wiley and Sons).

charge transfer, enhancing the conductivity of the sensor. The results revealed that oxygen ions get adsorbed on the metals (Au and Ag), metal oxide (WO_3) and CNT surface. When the sensor is exposed to NO_2 gas, the molecules accept electrons to form gaseous ions and react with chemisorbed oxygen, leading to an increase in resistance, and the corresponding reaction is as follows:

$$NO_2(g) + O_2^-(ads) + 2e \rightarrow NO_2^-(ads) + 2O^-(ads) \quad (2)$$

Besides the above-mentioned phenomenon, the formation of a Schottky barrier and p–p heterojunction between WO_3 and p-type CNT can affect the width of the depletion layers (DL) and eventually change the resistance during sensing. For the recovery of the sensor, UV-LED is used, where the sensor prevents the immediate recombination process, resulting in an improvement in the photocatalytic reaction, and consequently an increase in the sensitivity of sensor compared to that without UV irradiation. The corresponding reaction is as follows:

$$2NO_2(g) + e(h\nu) \rightarrow 2NO(h\nu) + O_2^-(h\nu) \quad (3)$$

The sensor showed 262% response at 500 ppb NO_2 under UV irradiation and the calculated limit of detection (LOD) was 45 ppb.

Further, for bendable NO_2 sensors, various CNT-polymer hybrids have been explored. In 2019, Kumar *et al.* reported NO_2 sensing using a polyethyleneimine (PEI)-functionalized SWCNT sensor.[93] The as-made sensor showed high sensitivity (37%) for 50 ppm NO_2 at room temperature with quick recovery time (240 s).

4.1.2 Sensing with graphene and its hybrid nanocomposites. Similar to CNTs, graphene also senses strong oxidizer gases, *i.e.*, NO_2 (shown in Table 3). In 2019, Ma *et al.* created defects on pristine graphene *via* Si^+ irradiation, and then transferred it to other pristine graphene layers grown on a germanium substrate.[80] The as-made sensing material showed a thirteen-times higher response than pristine monolayer graphene due to its high adsorption efficiency and strong interaction with the gas molecules, as explained theoretically. Besides graphene, GO and rGO have also been studied for NO_2 sensing, where the response of graphene-based sensors can be tuned by varying the concentration of oxygen-containing groups in GO and rGO.[94] Between them, rGO is mostly preferred for gas sensing applications because it possesses a larger number of defects, which act as adsorption sites for analyte molecules.[95] In this case, Sharma *et al.* (2019) compared the sensitivity of GO, chemically synthesized rGO (C-rGO), and green synthesized rGO (G-rGO) and reported that G-rGO (254.7%) and C-rGO (93.9%) showed higher sensitivity than GO (22.7%) towards 10 ppm NO_2 at 150 °C [96] given that G-rGO was highly reduced compared to C-rGO. Due to its high reduction level, a large concentration of defects in terms of high adsorption sites was observed in G-rGO. Moreover, Park *et al.* (2020) synthesized semiconducting rGO, which showed a high response (~32%) for 5 ppm NO_2 with an extremely low LOD.[97]

Although rGO has high sensitivity, it has irreversible recovery due to its cracked structure. Hence, to solve this issue, surface modification by decorating metal oxides such as ZnO, SnO_2, Co_3O_4, In_2O_3, CuO, and Fe_2O_3 together with graphene, GO, and rGO has been explored for enhancing its sensing performance.[82,83,99–102] In one of the works, Jyoti *et al.* synthesized a ZnO-decorated graphene-based sensor for NO_2 gas detection.[103] The as-made sensor showed 48.4% sensitivity for 40 ppm NO_2 at room temperature. In another work, Zhang *et al.* synthesized an NO_2 detector using SnO_2/rGO as the sensing material.[98] Furthermore, the sensor was exposed to four other gases (Cl_2, NO, CO, and H_2O) and showed selectivity towards NO_2 gas (shown in Fig. 7b).

Similar to other graphene derivatives, graphene quantum dots have also been explored for NO_2 sensing. In a recent study, Purbia *et al.* (2020) synthesized nitrogen-doped GrQD-functionalized SnO_2 *via* the wet chemical technique as a sensing material.[104] Subsequently, a sensor film was fabricated *via* spin coating. The as-made sensor could sense a very low concentration (~20 ppb) and showed an ultrahigh response ($R_g/R_a = 4336$) for 100 ppb NO_2 at 50 °C.

As shown in Table 3, rGO-based composites are the most explored CNMs towards NO_2 sensing given that they have easy synthesis procedures due to their good interaction with various MOs, MNPs, polymers and functional groups of rGO. However, although rGO is the most preferred, in terms of minimum detection limit, graphene (synthesized *via* CVD) is the most

Table 3 Comparative study of the parameters for significant works done on NO_2 sensing using CNM hybrid nanocomposite sensors

Sensing material	Analyte	Operating temperature	Response	Response time	Recovery time	Limit of detection	References
ZnO-decorated MWCNTs	10 ppm NO_2	300 °C	1.023[a]	93.1 s	285.2 s	—	Kwon *et al.* (2017)[65]
Polypyrrole–nitrogen-doped MWCNTs	5 ppm NO_2	RT	24.82%[b]	65 s	668 s	<0.25 ppm	Liu *et al.* (2019)[105]
Pd-MWCNTs	1 ppm NO_2	100 °C	10%[b]	~220 s	~1700 s	—	Dilonardo *et al.* (2017)[106]
Fe_2O_3-SWCNTs	20 ppm NO_2	RT	19%[b]	—	—	—	Hua *et al.* (2017)[107]
SWCNT-PTFE	0.75 ppm NO_2	RT	21.58%[b]	5 min	15 min	<0.75 ppm	Agarwal *et al.* (2018)[108]
	5 ppm NO_2		167.7%[b]				
f-SWCNTs with PEI	50 ppm NO_2	RT	37%[b]	240 s	—	—	Kumar *et al.* (2020)[93]
MWCNTs WO_3 decorated with Au–Ag	100 ppb NO_2	RT	28%[b]	267 s	—	45 ppb	Su *et al.* (2020)[8]
ZnO-SWCNTs	1000 ppm NO_2	150 °C	~900%[b]	70 s	100 s	—	Barthwal *et al.* (2018)[64]
ZnO-rGO	2.5 ppm NO_2	110 °C	33.11[a]	182 s	234 s	1.3 ppb	Cao *et al.* (2020)[99]
MoS_2-rGO	1 ppm NO_2	25 °C	6%[b]	360 s	720 s	4.4 ppb	Yi *et al.* (2020)[109]
SnS_2-rGO	8 ppm NO_2	RT	49.8%[c]	153 s	76 s	8.7 ppb	Wu *et al.* (2020)[19]
Graphene on SiC substrate	4 ppm NO_2		105.1%[b]	—	—	1 ppb	Yu *et al.* (2020)[110]
N-doped GrQDs-SnO_2	100 ppb NO_2	150 °C	292[a]	181 s	81 s	20 ppb	Purbia *et al.* (2020)[104]
		50 °C	4336[a]	528 s	384 s		
SnO_2 incorporated CuO-rGO	50 ppm NO_2	RT	~250%[b]	~90 s	~255 s	150 ppb	Bo *et al.* (2020)[111]
SnO_2-rGO:Pd	4 ppm NO_2	200 °C	185[a]	8 s	215 s	0.5 ppm	Bhangere *et al.* (2020)[101]
SnO_2-rGO hydrogel	5 ppm NO_2	RT	32.1%[c]	177 s	260 s	2.8 ppb	Wu *et al.* (2020)[37]
2.4 wt% rGO/Co_3O_4	5 ppm NO_2	RT	26.8%[b]	1.5 min	40 min	0.05 ppm	Zhang *et al.* (2018)[83]
Bilayer Gr	25 ppm NO_2	RT	38.9%[b]	—	—	—	Seekaew *et al.* (2017)[76]
Trilayer Gr	25 ppm NO_2		~19%[b]				
4 layers Gr	25 ppm NO_2		~12%[b]				
Monolayer	25 ppm NO_2		~16%[b]				
3 wt% rGO-In_2O_3	1 ppm NO_2	74 °C	1337[a]	208 s	39 s	10 ppb	Liu *et al.* (2017)[100]
MoS_2-Gr	10 ppm NO_2	200 °C	69%[b]	0.7 s	0.9 s	0.2 ppm	Hong *et al.* (2019)[112]
TiO_2–nitrogen-doped Gr QDs	100 ppm NO_2	RT	31.1%[b]	235 s	285 s	—	Murali *et al.* (2020)[113]
		250 °C	223%[b]				
Defected Gr-pristine Gr	100 ppm NO_2	25 °C	~2.45[d]	38 s	238 s		Ma *et al.* (2019)[80]
ZnO-rGO	40 ppm NO_2	RT	48.4%[b]	—	—	4 ppm	Jyoti *et al.* (2018)[103]
SnO_2-0.3% rGO	10 ppm NO_2	RT	2.021[a]	171 s	254 s	—	Gui *et al.* (2018)[114]
		200 °C	247.8[a]	39 s	15 s		
α-Fe_2O_3-12.2 wt% rGO	5 ppm NO_2	RT	8.2[a]	2.1 min	40 min	0.05 ppm	Zhang *et al.* (2018)[82]
Si-doped Gr	50 ppm NO_2	RT	21.5%[b]	126 s	378 s	18 ppb	Niu *et al.* (2021)[115]

[a] R_a/R_g (oxidizing gas) or R_g/R_a (reducing gas). [b] $\Delta R/R_a$. [c] $\Delta G/\Delta G_0$. [d] $\Delta I/I$.

interesting CNM (1 ppb). Simultaneously, SWCNT- and MWCNT-based nanocomposites also achieved a low LOD (45 ppb). Additionally, most of these CNMs show good responses even at room temperature.

4.2 CO_x sensors

CO_x (CO and CO_2) are toxic, odorless, and colorless pollutants, which are dangerous to human beings. Low exposure may only cause nausea, vomiting and dizziness. However, higher consumption of these carbon gases can be very dangerous because CO is toxic, and CO_2 is an asphyxiant at high concentrations, which can increase the risk of heart diseases. Hence, to reduce workplace injuries and accidents, gas detectors are required as safety measures. Additionally, CO_2 is the biggest factor influencing global warming. Specifically, the radiative force by CO_2 is increasing daily, which causes an imbalance in the received and radiated sunlight. Therefore, CO_x sensors are required for various applications, including environment monitoring and capnography.

4.2.1 Sensing with CNTs and their hybrid nanocomposites. MWCNTs are commonly studied for CO_x (CO and CO_2) sensing.[16] Kumar *et al.* synthesized a CNT film *via* vertically aligned CNT trees and the as-synthesized film was purified using nitric acid before CO_2 sensing.[73] When the MWCNT film was exposed to air, atmospheric oxygen (O_2) adsorbed on the CNT surface.

$$O_2(ads) + 3e \rightarrow O^{2-}(ads) + O^{-} \quad (4)$$

After the interaction of CO_2 gas with ionized oxygen, a metastable compound CO_3 was formed[41] and released

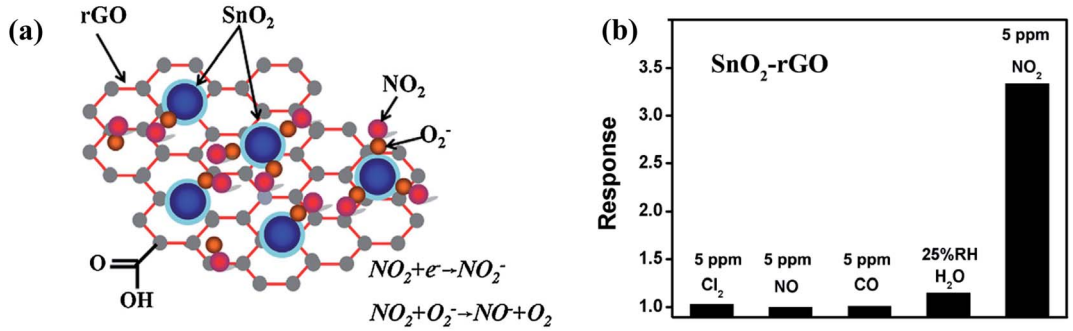

Fig. 7 (a) Illustration of the sensing mechanism for the gas sensor based on SnO_2/rGO nanohybrid. (b) Selectivity (calculated using R_g/R_a) histogram of SnO_2/rGO gas sensor to various gases at room temperature.[98] (reprinted from ref. 98, Copyright (2014), with permission from Elsevier).

electrons, which further increased the potential barrier, and consequently the resistance of the CNT film decreased.

$$CO_2 + O^{2-} \rightarrow CO_3 + 2e \quad (5)$$

However, at high exposure, the metastable compound can interact with itself (represented by eqn (6)). Hence, in this situation, less change in the resistance was observed.

$$CO_3 + CO_3 \rightarrow 2CO_2 + O_2(gas) \quad (6)$$

In one of the latest works, Ahmad *et al.* (2020) synthesized an MWCNT-alumina sensor *via* the sol–gel process (having various CNT concentrations of 0.6 wt%, 1.0 wt%, 1.5 wt%, 2.0 wt%, and 3.0 wt%) for the detection of CO_2.[116] The sensor having 2.0 wt% CNTs showed the highest response, and beyond this concentration, the sensing response gradually decreased due to the poor dispersion of the CNTs in the alumina matrix. As shown in Fig. 8, both physisorption and chemisorption phenomena occurred on the surface of the nanotubes. When CO_2 was injected into the sensing chamber, the electrons from CO_2 (reducing species) transferred to MWCNT (p-type). Due to charge delocalization, there was a shift in the energy band diagram. The calculated sensitivity ($\Delta R/R_a$) was 7.3% at 450 ppm CO_2 with a very short recovery time (14.15 s). For the desorption of the analyte molecules, external source UV light was used, decreasing the barrier height (ϕ_B) with a slight change from the original bandgap position (as illustrated in Fig. 8).

Another exciting work presented the sensing mechanism of CO on poly(diallyl)dimethylammonium chloride (PDDA) solution-coated MWCNTs (2020).[117] According to the described mechanism, there is a positive charge on the nitrogen atom in PDDA. When CO was introduced on the surface of the sensor, a charge transfer phenomenon occurred from CO to the quaternary NH_4^+ of PDDA. Due to this type of physisorption, the overall resistance of the sensor decreased and it eventually showed a high response. The highest sensitivity (11.51%) was achieved at 20 ppm CO.

4.2.2 Sensing with graphene and its hybrid nanocomposites. Similar to CNTs, CO_2 gas can also be sensed using graphene and functionalized graphene, where CO_2 can act as an electron donor and acceptor when adsorbed on the graphene

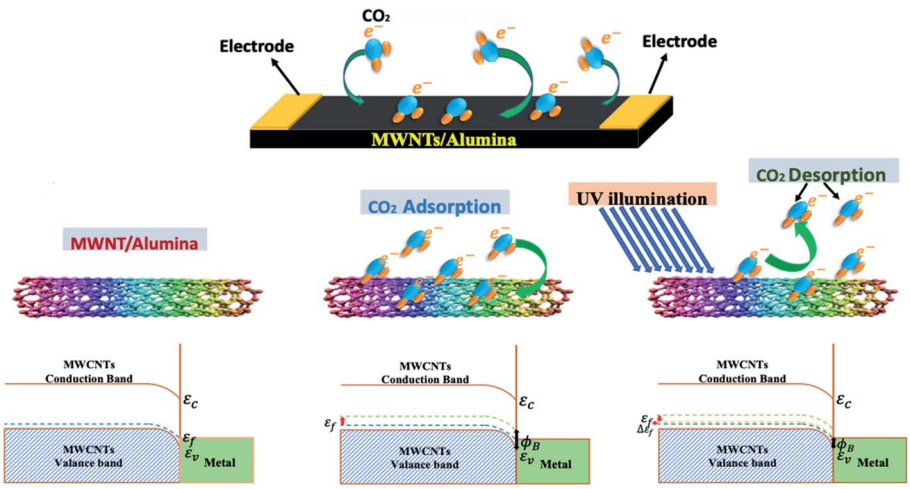

Fig. 8 Schematic representation of electron transfer on CNT surface and energy band diagram[116] (reprinted from ref. 116, Copyright (2017), with permission from Elsevier).

edge and adsorbed in the centre of the graphene sheets, respectively.[118] Moreover, graphene having zigzag edges has higher sensitivity for CO_2.[119,120] When CO_2 interacts with p-type graphene, electrons migrate from graphene, and consequently the hole concentration increases in graphene, leading to an increase in resistance. Karthik *et al.* synthesized rGO/TiO_2 composite films *via* the spray pyrolysis technique and used them as sensing materials for numerous gases such as H_2S, SO_2, and CO_2.[121] The as-made sensor showed the highest sensitivity (92%) towards CO_2, where the n–n heterojunction between rGO and TiO_2 is beneficial for a high sensing response. Furthermore, numerous calculations regarding CO and CO_2 have been implemented *via* DFT to study the interaction of graphene or doped graphene and gas molecules.[122–127] Fan *et al.* studied single- and double-layer graphene and concluded that single-layer graphene shows a higher response.[127] Recently, Salih *et al.* (2020) studied Pt-doped hydrogen and nitrogen armchair graphene nanoribbons (AGNR) for CO and CO_2 sensing theoretically.[128] After doping Pt, the adsorption energy increased up to thirteen and nine times that of H-AGNR and N-AGNR for CO and CO_2, respectively. However, numerous computational studies regarding CO_x sensing have been performed, more lab experiments should be done. A summary of CO_x sensors based on CNM hybrid composites is provided in Table 4.

It is observed that the research on CNMs-based CO_x detection sensors is less than that on other gases given that their pristine form shows a poor response towards CO_x gas. However, hybrid nanocomposites are studied comparatively more for CO sensing (observed from Table 4). Additionally, CNMs-based flexible sensors have attracted more attention given that the commercialized MO-based CO_x sensors have negligible flexibility.

4.3 CH_4 sensors

Environmental methane (CH_4) is a well-mixed ozone-depleting gas with the second biggest increment in radiative constraining after CO_2.[133] The major sources of CH_4 gas are natural gas production and burning of agriculture biomass. According to the global monitoring system, the mole fraction of methane determined from marine surface sites reached up to 1876.3 ppb, which is 1.01 times higher than the previous year (1865.3 ppb).[134] Furthermore, CH_4 is an odourless and colourless gas, which can be explosive upon mixing with ambient oxygen. Therefore, its presence even in small concentrations is a major threat and needs to be detected.

4.3.1 Sensing with CNTs and their hybrid nanocomposites. Some significant research has been performed on the detection of CH_4 using CNT-based nanocomposites. Kathirvelan *et al.* developed a methane detector having MWCNTs as the sensing element.[135] The recovery time was very short, about 60 s, due to the physisorption of CH_4 on the CNT surface, facilitating the easy removal of the analyte. For further improvement, Humayun *et al.* fabricated a CH_4 sensor *via* ZnO-functionalized MWCNTs[136] and explained a UV recovery-based plume mapping algorithm for the recovery of the sensor. For further enhancement, various metal ions and metals were doped in CNTs. One of the exciting works involves a methane gas sensor based on Li^+-doped CNTs as the sensing material and reported that CH_4 gas molecules are attracted to Li^+ for further interaction with CNTs.[137] Considering that Li^+ is electron deficient, more holes appeared in the Li^+/CNT film. Due to the change in the hole concentration of the CNTs, the sensor showed improved sensitivity (14.48% at 500 ppm CH_4). For a further improvement in the sensing performance, Wu *et al.* fabricated methane sensors based on lithium-montmorillonite (Li-MMT) or lithium cyclodextrin (Li-CD),[138] where Li-MMT showed a higher response (~42% @ 500 ppm CH_4).

In another work, an SnO_2–Pt/MWCNT-based sensor was synthesized and CH_4 gas was sensed. The three major reasons for the high performance of the as-made sensor are p–n heterojunction formation, high surface area, and spill-over effect at the Pt nanoparticles.[139] However, only few *ab initio* studies focusing on CNT-based methane sensors have been performed compared to other gases. Therefore, the understanding of the binding energy of CH_4 gas on the CNT surface and doped CNT surface still needs to be addressed. Simultaneously, various doped graphene nanostructures have been explored for CH_4 sensing either theoretically[140] or experimentally.

Table 4 Comparative study of the parameters for significant works done on CO_x sensing using CNM hybrid nanocomposite sensor

Sensing material	Analyte	Operating temperature	Response	Response time	Recovery time	Limit of detection	References
ZnO-MWCNT	25 ppm CO	70 °C	62%[a]	2 s	3 s	—	Özütok *et al.* (2019)[129]
Polyaniline-MWCNTs	500 ppm CO	RT	6.83%[a]	105 s	210 s	—	Roy *et al.* (2018)[130]
	1000 ppm CO		26.73%[a]	76 s	227 s		
MWCNTs-PDDA	1 ppm CO	RT	5.25%[a]	29 s	33 s	127 ppb	Roy *et al.* (2020)[117]
	20 ppm CO		11.51%[a]	18 s	45 s		
MWCNTs-alumina	450 ppm CO_2	RT	7.3%[a]	53.7 s	14.15 s	—	Ahmad *et al.* (2020)[116]
MWCNTs	5000 ppm CO_2	RT	210%[a]	30 s	49 s	—	Kumar *et al.* (2019)[73]
ZnO-rGO	1000 ppm CO	200 °C	85.2%[a]	7 s	9 s	<10 ppm	Ha *et al.* (2018)[50]
		RT	27.5%[a]	14 s	15 s		
rGO-Mn_3O_4	50 ppm CO	25 °C	70.8%[a]	3 s	6 s	—	John *et al.* (2020)[131]
	4 ppm CO	200 °C	77.8%[a]	2 s	5 s	4 ppm	
0.1 Pd-doped SnO_2-Gr	30 ppm CO	250 °C	99%[a]	0.3 s	0.3 s	—	Debataraja *et al.* (2019)[132]

[a] $\Delta R/R_a$.

4.3.2 Sensing with graphene and its hybrid nanocomposites. Besides CNTs, graphene has also been used to develop CH_4 gas sensors. In 2018, SnO_2 nanorod-decorated graphene sheets were studied for CH_4 detection.[45] As the reported sensing mechanism, the metal oxide interacts with oxygen in the air, leading to the formation of oxygen ion species (O^{2-}, O^- and O_2^-), which chemisorb on the MO surface.[30] When the sensor is exposed to a CH_4 atmosphere, the pre-adsorbed oxygen ions interact with the gas molecules and release electrons (presented by eqn (7) and (8)), resulting in high sensitivity (illustrated in Fig. 9a).

$$CH_4 + 4O^-(ads) \rightarrow 2H_2O + CO_2 + 4e \quad (7)$$

$$CH_4 + 2O_2^-(ads) \rightarrow 2H_2O + CO_2 + 4e \quad (8)$$

The other explained sensing phenomenon is based on oxygen vacancies, which influence the sensor response[141] for the detection of CH_4 gas.

$$2V_O^{\bullet} + O_2(gas) + 2e \rightarrow 2O_{Ox} \quad (9)$$

$$CH_4(gas) + 4O_{Ox} \rightarrow CO_2(gas) + 2H_2O(gas) + 4V_{Ox} \quad (10)$$

$$V_{Ox} \rightarrow 2V_O^{\bullet} + e \quad (11)$$

where V_{Ox}, O_{Ox} and $V_O^{\bullet}$ are shallow neutral oxygen vacancy, oxide anion healing of oxygen vacancy, and singly ionized oxygen vacancy, respectively. SnO_2 shows in-plane oxygen vacancies,[142] which promote the detection of CH_4. The as-made sensor showed 24.9% response at 1000 ppm CH_4 at 150 °C. Fig. 9b shows the stability of the as-made sensor even after 30 days.

Further, Ag NP-decorated graphene-based smart sensing material was studied for CH_4 sensing.[87] The oxygen ions were chemisorbed on the Ag NPs and graphene and the WF of G + O_2 was less than that of Ag NPs + O_2 (as shown in Fig. 9c and d, respectively). During gas sensing, electrons move from Ag NPs + O_2 to G + O_2, which shifts the E_F of Ag + O_2 owing to the increase in the hole concentration of graphene and directly influences the response of the sensor. Some significant works on CH_4 sensors using CNMs-based hybrid nanocomposites are shown in Table 5.

It has been reported that unfunctionalized and metal-decorated SWCNTs exhibit a very low response towards CH_4 at room temperature.[147] Therefore, MWCNT hybrid nanocomposites have attracted more attention than SWCNTs. Moreover, rGO has also been explored. Among all the mentioned sensors in Table 5, the TiO_2-rGO-based sensors showed the highest response (96.93%) even at a low concentration (800 ppm CH_4).

4.4 NH_3 sensors

Ammonia (NH_3) is a colorless gas with a strong smell, which has been used as a refrigeration gas for centuries. Although it has no global warming potential or impact on the ozone level, it is still essential to detect it given that a large number of people is exposed to ammonia gas by breathing its vapors from many

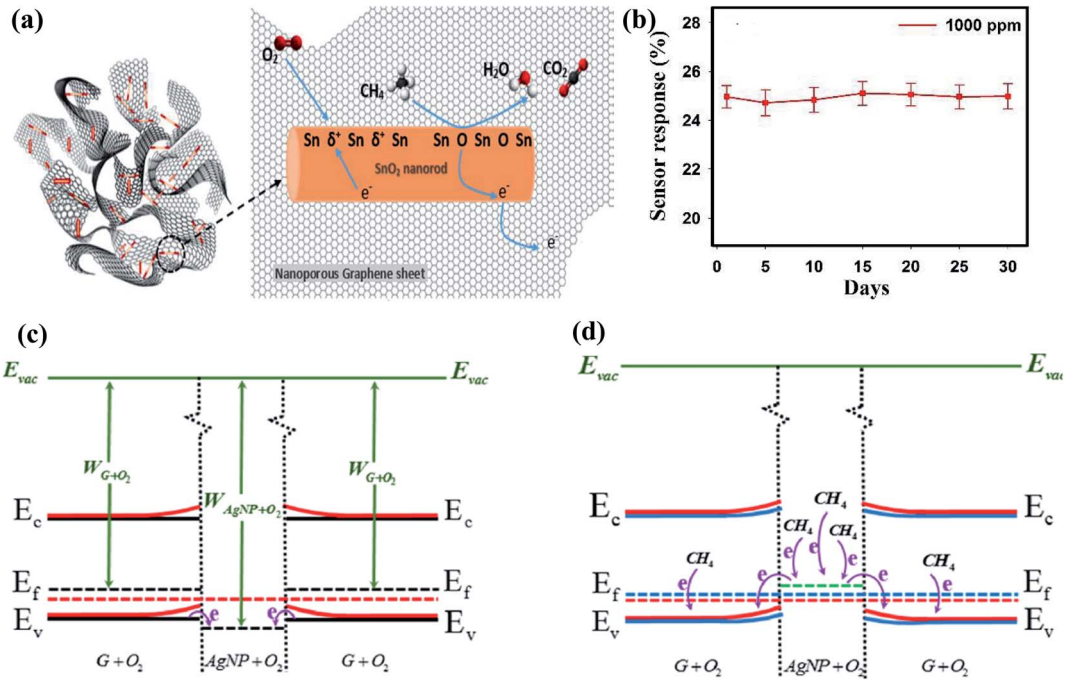

Fig. 9 (a) Schematic representation of sensing mechanism for CH_4 detection on SnO_2-graphene-based sensor. (b) Stability graph of sensor (response calculated using $\Delta R/R_a$)[45] (reprinted from ref. 45, Copyright (2017), with permission from Elsevier). (c) Schematic illustration of the energy band diagrams for preabsorbed graphene and Ag NPs under ambient conditions. (d) Electron transfer upon exposure to CH_4 (ref. 87) (reprinted with permission from ref. 87. Copyright (2019) American Chemical Society).

Table 5 Comparative study of the parameters for the significant works done on CH_4 sensing using CNM hybrid nanocomposite sensors

Sensing material	Analyte	Operating temperature	Response	Response time	Recovery time	Limit of detection	References
V_2O_5 filled in MWCNTs	40 ppm CH_4	RT	1.5%	~16 s	~120 s	—	Chimowa *et al.* (2017)[143]
MWCNTs decorated with SnO_2–Pt	100 ppm CH_4	RT	28.25%[a]	176 s	763 s	490 ppb	Navazani *et al.* (2020)[139]
	10 000 ppm CH_4		94.26%[a]	122 s	1178 s		
Li ion doped CNT	500 ppm CH_4	RT	14.48%[a]	—	—	—	Chen *et al.* (2018)[137]
TiO_2 nanotubes-rGO	800 ppm CH_4	25 °C	96.93%[a]	~18 s	~61 s	10 ppm	Acharyya *et al.* (2016)[144]
SnO_2-rGO/PANI	100 ppm CH_4	RT	26.1%[a]	360 s	1150 s	—	Navazani *et al.* (2018)[145]
PbS-3.5 wt% rGO	100 ppm CH_4	RT	45%[a]	92 s	65 s	—	Roshan *et al.* (2019)[146]

[a] $\Delta R/R_a$.

cleaning products. The major drawback of ammonia is that it can be flammable at high concentrations. Besides, its low concentration inhalation leads to coughing and soreness to the nose given that it has a very suffocating smell, and beyond a certain concentration, it can cause burning sensation to the nose and throat. Furthermore, in extreme cases, it may damage the respiratory system completely. Besides the olfactory sense, skin, and eyes are affected, while NH_3 gas interaction at low levels and higher levels it can cause burns and blindness, respectively. Vytenis documented a real incident of an NH_3 explosion, which happened in West Texas in 2013, killing 15 people and injuring 200.[148] Furthermore, NH_3 gas reacts with water exothermically, and ammonia corrosion occurs in many metals such as Zn and Cu, and their alloys. Therefore, its detection is necessary.

4.4.1 Sensing with CNTs and their hybrid nanocomposites. Significant research on the detection of NH_3 using CNT-based chemiresistive sensors has been performed.[149–154] In one of the studies, Ansari *et al.* observed that SWCNTs functionalized using nitric acid (f-SWCNTs) showed a higher response than pristine SWCNTs[153] together with a long recovery time due to the strong chemical bonding of the gas molecules with the functional groups of SWCNTs. In another work, Schütt and coworkers synthesized tetrapodal ZnO networks (ZnO-T) decorated with MWCNTs as an NH_3 sensing material.[155] In ambient atmosphere, oxygen molecules were adsorbed on the ZnO surface owing to the EDR at the T-arms of ZnO (shown as blue colour in Fig. 10a).

$$O_2(ads) + 2e \rightarrow O^{2-}(ads) \quad (12)$$

When NH_3 gas came in contact with the sensing material, the chemisorbed oxygen ions acted as adsorption sites for the target gas and the released electrons tuned the bandgap.

$$2NH_3 + 3/2O^{2-} \rightarrow N_2 + 3H_2O + 3e \quad (13)$$

Consequently, the width of the depletion region decreased, leading to a decrease in ϕ_B (shown in left section of Fig. 10b). However, when 2 wt% and 4 wt% CNTs (seen in Fig. 10c and e, respectively) were coated on ZnO-T, electrons transferred from the reducing analyte to the CNTs very rapidly, and thus to ZnO-T (illustrated in Fig. 10d). Therefore, they helped to enhance the sensing response.

The sensing at a high concentration of CNTs (>2 wt%) had a negative effect on the sensitivity of ZnO-T given that the CNTs were accumulated on the ZnO arms, which decreased the number of adsorption sites (shown in Fig. 10f). Further, Guo *et al.* (2018) studied Fe_3O_4/CNTs as a sensing material for NH_3 gas,[156] where the explained sensing mechanism is based on magnetic catalysis and chemical bonding. Magnetite has ferrous (Fe^{2+}) and ferric (Fe^{3+}) atoms. When ammonia is exposed to the surface of the sensing material, the analyte molecules are adsorbed on it. The H atoms in NH_3 bond chemically with the O atom of Fe_3O_4 (shown in Fig. 11). Moreover, the N atoms shared electrons with the Fe_3^+ atom. Therefore, together with chemical bonding, the magnetic effect of Fe_3O_4 was also beneficial for analyte adsorption. The effect of an external magnetic field on the sensitivity is described by the following equation:

$$S = M \times e^{\lambda \times B2} \quad (14)$$

where S and B are the sensitivity and magnetic field intensity, respectively, and M and λ are the constants of the gas adsorption reaction.

However, besides Fe_3O_4, CNTs provide adsorption sites, resulting in high sensitivity. The overall sensitivity was enhanced because of the high adsorption capacity of Fe_3O_4.

Another CNT hybrid nanocomposite for NH_3 sensing is the CNT–polymer matrix, where conducting polyaniline (PANI) is commonly used.[157–159] Zhang *et al.* described the synergistic effect of PANI coated on an MoS_2-functionalized MWCNT nanomaterial.[160] The as-made sensor showed 49.66% sensitivity at 10 ppm NH_3. According to the described model, when PANI is exposed to NH_3 gas, electrons get transported from NH_3 to PANI, forming NH^{4+}. In addition, MWCNTs also react in the similar manner. Besides, the formation of a p–n heterojunction between p-type PANI and n-type MoS_2 helped to improvise the sensing response of the as-made sensor. In another work with

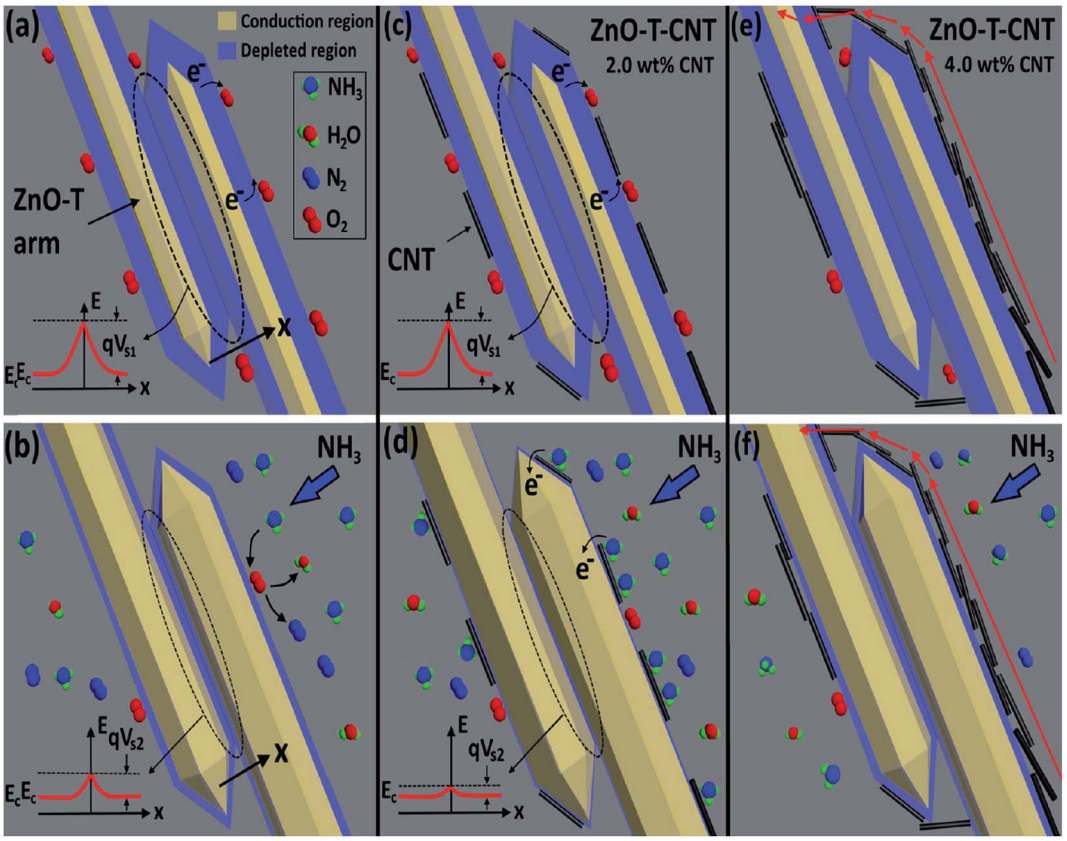

Fig. 10 Illustration of sensor in air (a) ZnO-T, (c) ZnO-T-2 wt% CNT networks and (e) ZnO-T-4 wt% CNT networks and in NH_3 atmosphere (b) ZnO-T, (d) ZnO-T-2 wt% CNT networks and (f) ZnO-T-4 wt% CNT networks[155] (reprinted with permission from ref. 155. Copyright (2017) American Chemical Society).

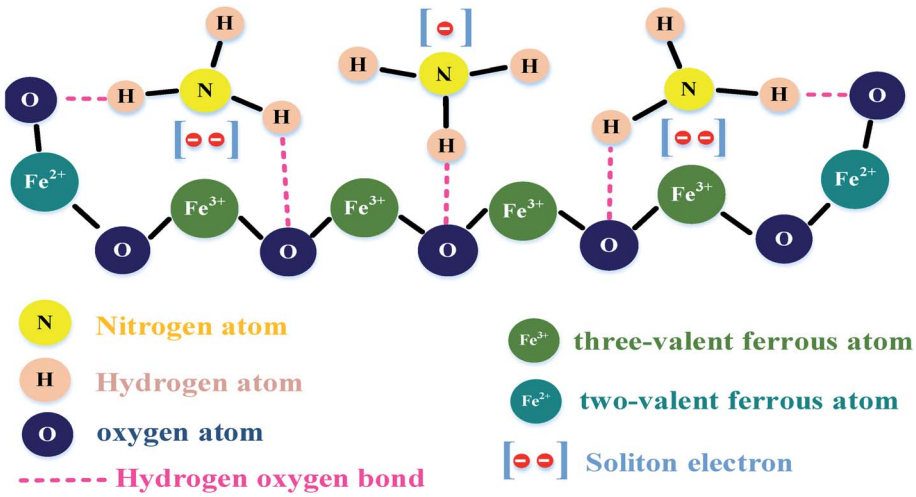

Fig. 11 Model of the intermolecular binding force[156] (reprinted with permission from ref. 156. Copyright (2018), MDPI Publisher, under Creative Commons Attribution 4.0 International License).

PANI-CNT for NH_3 sensing, Ansari *et al.* synthesized a carboxyl-functionalized SWCNT-wrapped polyaniline nanofiber (PANI) composite *via* the *in situ* chemical oxidative polymerization technique[90] and proposed the same sensing mechanism. When NH_3 comes in contact with the reactive site of PANI and f-CNTs, the electrons transfer from the reducing gas to PANI and f-SWCNTs, resulting in an enhancement in the resistance of the sensor. The sensing response of the as-made PANI@f-SWCNT (24–25%) was higher than that of the pristine (5–6%) and functionalized SWCNTs (18–20%) towards 10 ppm NH_3 due

to the high availability of adsorption sites. Although the sensing performance of PANI@f-SWCNT was lower than that of PANI-MoS_2@f-MWCNTs and its recovery time was much shorter. Moreover, less steps were involved in the synthesis of PANI@f-SWCNT compared to PANI-MoS_2@f-MWCNTs, where MoS_2 was synthesized *via* the hydrothermal route.

4.4.2 Sensing with graphene and its hybrid nanocomposites. Similar to other gases, graphene and functionalized graphene have also been explored for ammonia sensing.[161–163] Khurshid *et al.* studied NH_3 adsorption on a GO-based gas sensor.[48] When NH_3 gas molecules interact with GO, the charges get transferred from NH_3 to GO, influencing the charge carrier density of GO, and thus decreasing the resistance of the sensor. The molecular interaction between NH_3 gas and the hydroxyl group (OH) of GO occurs either *via* the coordination of N and H (OH…N having an interaction energy of 6.9 kJ mol^{-1}) or H and O from NH_3 and the hydroxyl group (NH…O having an interaction energy of 11.9 kJ mol^{-1}), respectively. Furthermore, NH_3 can interact with the carbonyl group (C=O…H–NH_2 having an interaction energy of 46.0 kJ mol^{-1}). Due to these interactions, the GO sensing device responded efficiently towards NH_3 gas. Further, Srivastava *et al.* reported NH_3 sensing on pure few-layer graphene (PFLGr) and boron-doped few-layer graphene (BFLGr).[78] The adsorption energy for NH_3 gas on BFLGr is higher than that on PFLGr given that the N atom of NH_3 gets easily attached to B atoms (shown in Fig. 12a). Therefore, boron-doped graphene as a sensing material showed higher sensitivity (~4 times higher than PFLGr) towards 32 ppm NH_3. The BFLGr sensor showed high repeatability even after 25 days (shown in Fig. 12b).

In a recent work, Ghule *et al.* (2021) studied various metal oxide (NiO, ZnO, and Bi_2O_3)-doped GO sensors and concluded that the Bi_2O_3-GO (81.23%) sensor exhibits the maximum response at 50 ppm NH_3 in comparison with ZnO-GO (60%), NiO-GO (20%) and pristine GO (~3–4%).[86] The sensing

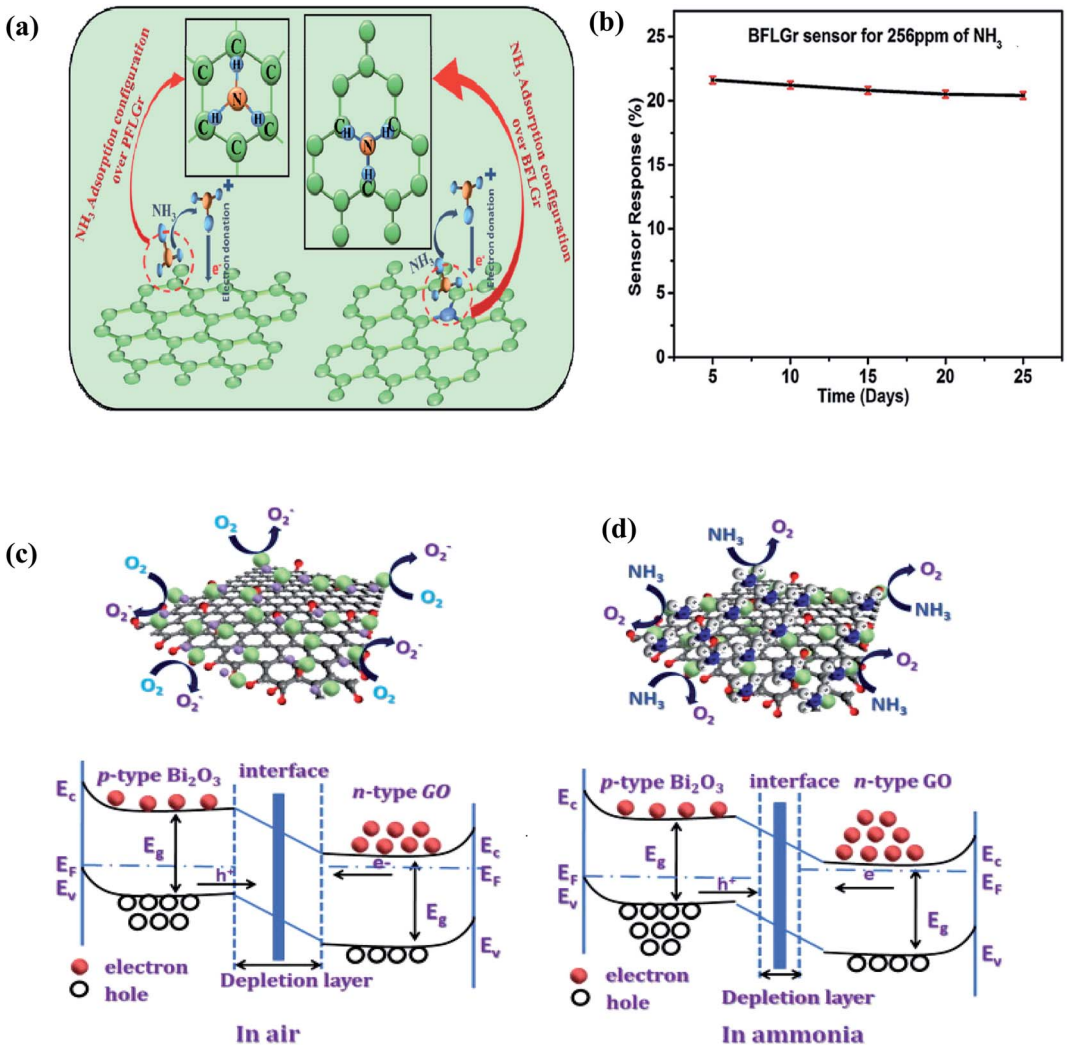

Fig. 12 (a) Schematic illustration of NH_3 adsorption and proposed gas sensing mechanism of the PFLGr and BFLGr sensor. (b) Plot of sensor response for a period of 25 days[78] (reprinted with permission from ref. 78. Copyright (2020), The Royal Society of Chemistry). Representation and band diagram of Bi_2O_3-doped graphene oxide in (c) air and (d) ammonia[86] (reprinted from ref. 86, Copyright (2021), with permission from Elsevier).

mechanism is based on the reduction of the DL width, as explained in Fig. 12d.

Another work employed zeolite imidazole framework-rGO (ZIF-67-rGO) as a sensing material for NH_3 gas, which was synthesized *via* the hydrothermal process.[164] When the reducing gas (NH_3) passed through the sensing chamber, the charge transferred from ZIF-67 (WF = 1.98 eV) to rGO (WF = 1–1.69 eV). Therefore, the DL width was reduced, and consequently the resistance decreased. On the contrary, the sensing mechanism is different to that of p-type CNTs given that the resistance should increase after NH_3 adsorption because ZIF-67-rGO acts as an n-type semiconductor. Table 6 presents the significant works performed on NH_3 sensors synthesized using CNM hybrid nanocomposites.

According to the information in Table 6, it can be concluded that the LOD value of CNMs-based composite for NH_3 gas sensors is generally very low (in the ppb range). In addition, most of the ammonia gas sensors having CNMs as the sensing material show good sensitivity at ambient temperature. The sensor made with TiO_2-decorated rGO has the highest response ($\Delta R/R_a = 170$).

4.5 H_2 sensors

Hydrogen (H_2) is a non-toxic, non-radioactive, and non-polluting gas, producing no hazardous combustion products, but under certain conditions such as 18–59% mixing in air, it becomes highly explosive given that it requires a low ignition energy, and thus can be extremely dangerous. Moreover, H_2 is a colourless and odourless gas, and therefore it is impossible to detect it without any detection device given that free hydrogen is highly reactive. It is ten times more flammable and even twenty times more explosive than gasoline. Also, the flames of fires caused by H_2 are invisible, which makes it a serious hazard to work with. Moreover, the H_2 explosion limit is confinement dependent, which can create a blast wave that can destroy nearby buildings and injure people. Therefore, a significant number of investigations on hydrogen stations have focused on its ignition, deflagration, and detonation. Recently, in 2019, a hydrogen explosion occurred in a US silicone plant in Waukegan, IIlinois.[174] According to the US Chemical Safety and Hazard Investigation Board, the plant lacked was hydrogen detectors. Therefore, precise hydrogen detectors are highly required.

4.5.1 Sensing with CNTs and their hybrid nanocomposites. The sensing of H_2 has been done significantly with MWCNTs. Recently in 2019, Guo *et al.* detected H_2 using a semiconducting CNT network as a transparent and flexible sensing material.[175] In the same year, Park *et al.* sensed H_2 on MWCNTs and crumpled MWCNTs on a PET and polystyrene (PS) substrate, respectively, and observed that the crumpled CNTs showed 3.25 times higher sensitivity than MWCNTs.[176]

Moreover, it has also been reported that for the enhancement of the sensing response towards H_2 gas, the presence of functionalized groups on the surface of CNTs such as COOH and OH plays a crucial role.[177] Furthermore, together with CNTs, Pd is generally used due to its high catalytic activity towards H_2 gas.[84,178,179] In 2018, Xiao *et al.* performed H_2 sensing on Pd nanoparticle (Pd NP)-decorated SWCNTs.[180] When H_2 is exposed to the Pd-decorated CNTs, it would interact in two

Table 6 Comparative study of the parameters for significant works done on NH_3 sensing using CNM hybrid nanocomposite sensors

Sensing material	Analyte	Operating temperature	Response	Response time	Recovery time	Limit of detection	Reference
WO_3 nanobricks-1 wt% CNT	30 ppm NH_3	50 °C	12.5%[a]	210 s	330 s	150 ppm	Le *et al.* (2019)[165]
	10 ppm NH_3	RT	6.8%[a]				
Pd-MWCNTs	1000 ppm NH_3	100 °C	32%[a]	—	—	—	Dilonardo *et al.* (2017)[106]
PANI-CNT	10 ppm NH_3	RT	~610%[a]	85 s	20 s	<200 ppb	Xue *et al.* (2017)[88]
f-SWCNTs-PANI	10 ppm NH_3	RT	24–25%[a]	1–4 s	8–10 s	—	Ansari *et al.* (2020)[90]
f-SWCNTs with HNO_3			18–20%[a]	9–10 s	30–32 s		
p-SWCNTs			5–6%[a]	12–15 min	40–42 min		
f-MWCNTs with red-phenol	100 ppm NH_3	—	18–23.2%[a]	6–8 s	30–50 s	—	Saxena *et al.* (2020)[166]
Polypyrrole – f-CNTs with NH_2	0.1 ppm NH_3	RT	525%[a]	138 s	465 s	0.04 ppb	Hamouma *et al.* (2018)[167]
Graphene oxide	100 ppm NH_3	RT	45%[a]	24 s	18 s	—	Khurshid *et al.* (2020)[48]
CrO_3 intercalated multilayer Gr	50 ppm NH_3	180 °C	54%[a]	10 s	20 s	—	Jaiswal *et al.* (2020)[162]
AgNPs-rGO	0.1 ppm NH_3	RT	—	5 s	6 s	1.2 ppb	Karaduman *et al.* (2017)[168]
	1 ppm NH_3		6.52%[a]				
PtNPs-rGO	0.1 ppm NH_3	RT	—	7 s	8 s	16 ppb	Karaduman *et al.* (2017)[168]
	1 ppm NH_3		2.87%[a]				
AuNPs-rGO	0.1 ppm NH_3	RT	—	13 s	17 s	1.6 ppb	Karaduman *et al.* (2017)[168]
	1 ppm NH_3		0.5%[a]				
Au GNRs	25 ppm NH_3	RT	34%[a]	224 s	178 s	—	Seifaddini *et al.* (2019)[169]
75 mM meta toluic acid functionalized GO	100 ppm NH_3	RT	12.2%[a]	60 s	80 s	—	Kumar *et al.* (2020)[170]
WS_2-rGO	10 ppm NH_3	33.5 °C	121%[a]	60 s	300 s	—	Wang *et al.* (2018)[171]
TiO_2-rGO	10 ppm NH_3	RT	170[a]	114 s	304 s	—	Ye *et al.* (2017)[172]
MWCNT-Gr hybrid film	300 ppm NH_3	RT	—	40 s	96 s	—	Bisht *et al.* (2014)[173]

[a] $\Delta R/R_a$.

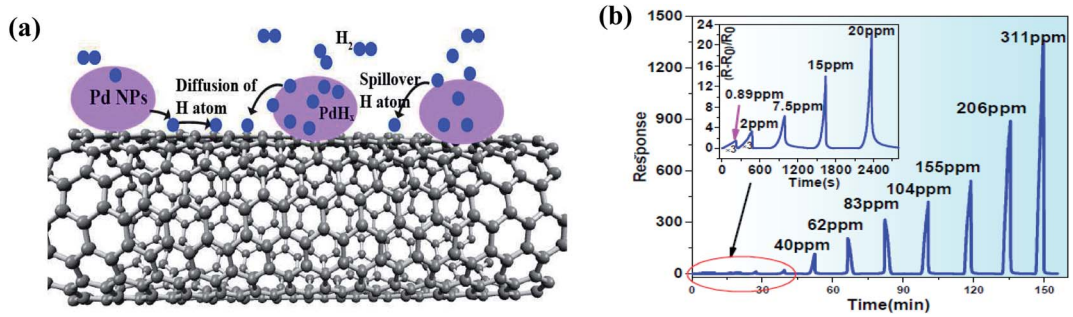

Fig. 13 (a) Schematic of H_2-Pd-CNT interaction on CNT surface. (b) Response to different H_2 concentrations at ambient temperature[180] (adopted with permission from ref. 180. Copyright (2018) American Chemical Society).

ways, either as H_2 dissolved in Pd to decrease the WF of Pd (electron transfer from Pd to CNTs) or H_2 dissociated on the Pd NPs to initiate the spill-over of H atoms (Fig. 13a). The spill-over H atoms diffuse on the surface of the CNTs and directly donate electrons to the CNTs, inducing a delocalized EDR, and thus increasing the resistance. The reactions occurring during exposure to H_2 are as follows:

$$H_2 \rightarrow 2H_{\text{atom on surface}} \rightarrow H_{\text{atom in Pd}} \quad (15)$$

$$O_2 + 2H_{\text{atom on surface}} \rightarrow 2OH,\ OH \rightarrow H_2O \quad (16)$$

Fig. 13b shows the response at different concentrations (0.89–311 ppm) of H_2 gas, where the sensor showed a much higher response (>1200) at 311 ppm.

Similar to Pd, Pt is also very encouraging due to similar phenomena.[181] One of the early research works was on Pt-doped TiO_2@F-CNTs for H_2 gas sensing.[182] Besides the catalytic effect of functionalized CNTs, the Schottky barrier formed at the boundary of Pt and TiO_2 also leads to electron transfer from Pt to TiO_2, and then from TiO_2 to CNTs, and these electrons produce E–H pairs in the CNTs, which consequently increase the overall resistance. Moreover, when H_2 gas molecules interact with Pt, they dissociate into hydrogen ions (H^+ and H^-), and then diffuse into Pt. The sensitivity of the f-MWCNTs-TiO_2-Pt based sensor was 1.35, 2.53, 4.75, and 19 times higher than that of f-MWCNTs-TiO_2-Pt, f-MWCNTs-Pt, f-MWCNTs and pristine MWCNTs, respectively.

4.5.2 Sensing with graphene and its hybrid nanocomposites. Numerous works have been performed on graphene-based hydrogen sensors.[183–186] Kamal *et al.* fabricated an H_2 sensor having rGO decorated with NiO as a sensing material.[187] The as-made sensing material (129.38 $m^2\ g^{-1}$) had a 3.7-fold higher surface area than NiO (26.33 $m^2\ g^{-1}$), due to the presence of rGO. Upon exposure to the analyte gas, the various chemisorbed oxygen ions reacted with hydrogen ions and released electrons by removing H_2O, which led to the formation of EDR. Moreover, the functional groups present on rGO also acted as active sites for the adsorption of gas molecules.

Another existing work explains the sensing mechanism of graphene decorated with Pd–Ag NPs.[188] Physisorption and chemisorption occur during H_2 sensing, where chemisorption occurs due to the formation of strong metal hydrides (Pd–H) having covalent bonds.[189] Recently, Achary *et al.* proposed $ZnFe_2O_4$–Pd decorated rGO as an H_2 sensing material.[190] The as-fabricated sensor showed a high response of 11.43% towards 200 ppm H_2 at room temperature. Fig. 14 shows the possible sensing mechanism of the sensor.

Due to the high surface availability and high charge mobility of rGO, the sensor showed a high response. Table 7 shows the various CNM hybrid nanocomposite-based sensors for H_2 gas.

As observed, Pd- and Pt-doped CNMs show high sensitivity towards H_2 gas given that these MPs show chemical sensitization based on the spill-over mechanism. To the best of our knowledge, Pd-CNTs show an ultrahigh response for H_2 sensing (~100 000%).

4.6 H_2S sensors

Dihydrogen sulphide (H_2S) is a colourless, flammable gas that smells like rotten eggs. Hence, it can affect the eyes, smelling sense and respiratory system. Long-duration exposure to H_2S can even paralyse the nervous system. Therefore, detectors are needed for H_2S. A level of H_2S gas at or above 100 ppm is lethal according to the IDLH values. Additionally, this gas is a silent threat, often invisible to the body's senses.

4.6.1 Sensing with CNTs and their hybrid nanocomposites. SWCNTs and MWCNTs have been explored for H_2S sensing. In 2017, Hua *et al.* synthesized an SWCNT-Fe_2O_3 flexible sensor for H_2S sensing[107] (shown in Fig. 15a). The sensing mechanism of H_2S gas by the SWCNT-Fe_2O_3 sensor can be explained by eqn (17).

$$2H_2S(g) + 3O_2^-(ads) \rightarrow 2H_2O(g) + 2SO_2(g) + 3e \quad (17)$$

The released electrons are adsorbed on the surface of the Fe_2O_3 NPs, and then transferred to the SWCNT film, where the E–H recombine, leading to a decrease in the concentration of hole carriers in the SWCNTs, which increases the resistance of the gas sensor.

Fig. 15b represents the response of the sensor towards 1 ppm to 100 ppm H_2S.

Srivastva *et al.* (2019) analysed zigzag pristine, boron and nitrogen-doped (10,0) SWCNTs using the Atomistix Toolkit-

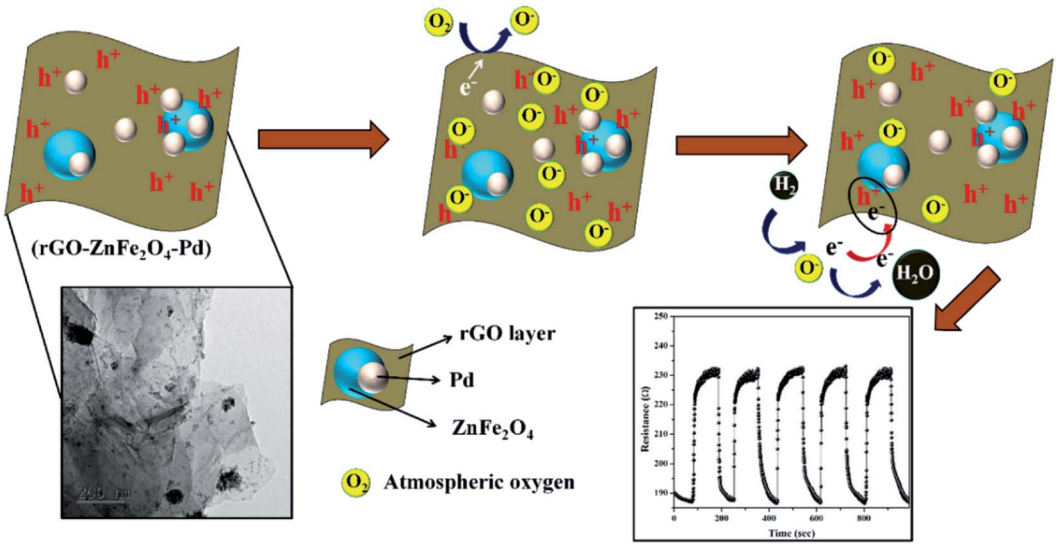

Fig. 14 Plausible sensing mechanism of $ZnFe_2O_4$–Pd decorated rGO towards H_2 gas[190] (reprinted from ref. 190. Copyright (2020), with permission from Elsevier).

Table 7 Comparative study of the parameters for significant works done on H_2 sensing using CNM hybrid nanocomposite sensors

Sensing material	Analyte	Operating temperature	Response	Response time	Recovery time	Limit of detection	Reference
MWCNT decorated with Pd	4% H_2	—	35.30%[a]	—	—	—	Yan *et al.* (2019)[191]
Pd-CNTs	311 ppm H_2	RT	100 000%[a]	7 s	89 s	0.89 ppm	Xiao *et al.* (2018)[180]
f-CNT with COOH and OH	10% H_2	RT	5.7%[a]	35 s	55 s		Han *et al.* (2019)[192]
Acidic-MWCNTs-TiO_2-Pt	0.05% H_2	RT	3.9%[a]		20 s	—	Dhall *et al.* (2017)[182]
Pt–Gr like carbon wrapped CNTs	4% H_2 in air	RT	42.8%[a]	120 s	—	<0.1%	Baro *et al.* (2018)[193]
MWCNTs	10% H_2	—	0.4%[a]	—	—	7100 ppm	Park *et al.* (2020)[176]
Crumped MWCNTs	10% H_2		1.3%[a]			2700 ppm	
Au-Gr	500 ppm H_2	—	5.46%[a]	16 s	274 s	—	Kim *et al.* (2019)[194]
Pt-rGO	0.5% H_2	50	8%[a]	63 s	104 s	—	Lu *et al.* (2018)[195]
Pt decorated ZnO-rGO	400 ppm H_2	100	99[a]	12 s	412 s	—	Drmosh *et al.* (2019)[196]
CuO-rGO	1500 ppm H_2	RT	~11%[a]	< 80 s	< 60 s	10 ppm	Zhang *et al.* (2017)[197]

[a] $\Delta R/R_a$.

Virtual NanoLab (ATK-VNL) simulation software.[198] The computational results of H_2S adsorption on the pristine SWCNTs (80.16%) showed the highest sensitivity and lowest recovery time compared with B-doped (60.79%) and N-doped CNT (78.76%). Further, Nobari *et al.* studied amide-functionalized SWCNTs as an H_2S sensor computationally

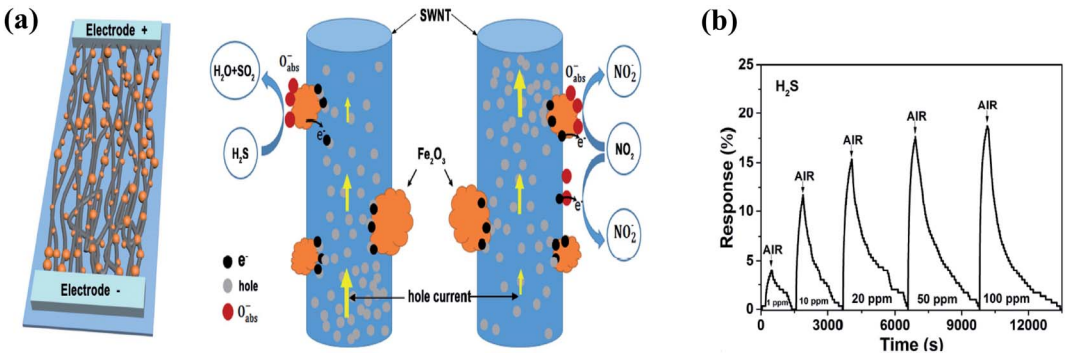

Fig. 15 (a) Schematic of the gas sensor based on SWNT-Fe_2O_3 composite film and schematic explaining the H_2S sensing mechanism. (b) Response ($\Delta R/R_a$) and recovery curves of sensor upon exposure to H_2S (1, 10, 20, 50, and 100 ppm) with complete recovery[107] (reprinted from ref. 107, Copyright (2017), with permission from Elsevier).

using the AVAGADRO software[199] and reported the maximum sensitivity of 89.3% at 40 mV.

Together with SWCNTs, MWCNTs have also been explored for H_2S sensing applications. Ibrahim *et al.* dissolved different concentrations of MWCNTs (0.01 and 0.1 mg mL^{-1}) in poly(2-methoxy-5-(2′-ethythexyloxy)-1,4-phenylenevinylene) films, which were studied for H_2S sensing.[200] The sample having a higher content of MWCNTs showed higher sensitivity

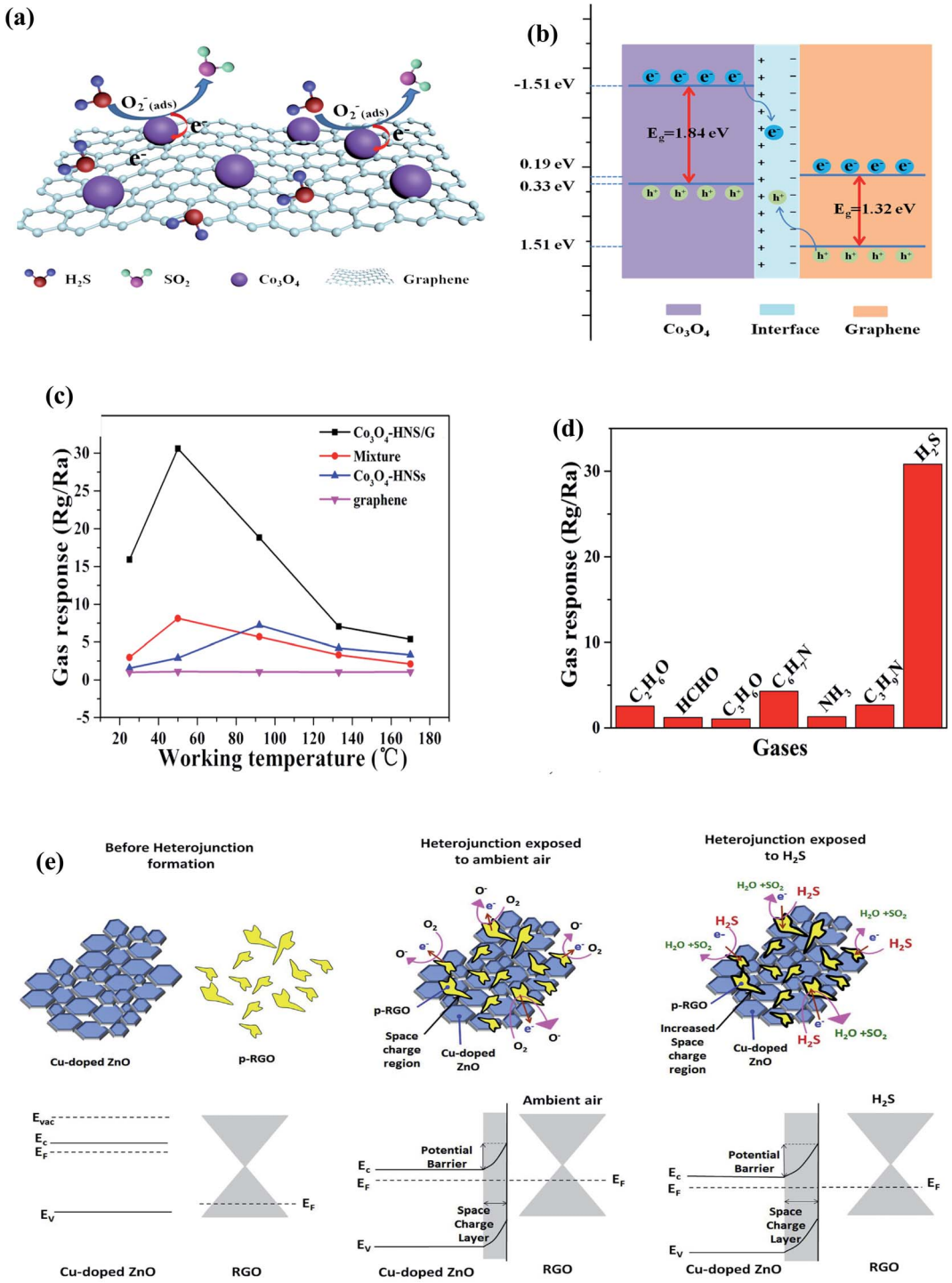

Fig. 16 (a) Schematic depiction of the sensing mechanism of the sensor, (b) energy band structure for the heterojunction of Co_3O_4 and graphene, (c) responses of Co_3O_4-HNS/G, Co_3O_4-HNSs, and graphene *versus* various operating temperatures to 50 ppm of H_2S and (d) plot of sensor constructed by Co_3O_4-2HNS/G to different gases with a concentration of 50 ppm at 50 °C (ref. 205) (adopted with permission from ref. 205. Copyright (2019) American Chemical Society). (e) Energy band diagram of Cu-doped ZnO/rGO nanocomposite[206] (reprinted from ref. 206, Copyright (2020), with permission from Elsevier).

(104.45%) in comparison with the sample having less content of CNTs (11.70%) given that it provides more adsorption sites.

4.6.2 Sensing with graphene and its hybrid nanocomposites. In the last five years, numerous H_2S sensors have been synthesized using graphene hybrid nanocomposites.[201–204] Liu *et al.* fabricated Co_3O_4 hollow-nanosphere/graphene (Co_3O_4-HNS/G) composites (shown in Fig. 16a) and used them as sensing materials for H_2S gas.[205] Due to the chemisorbed oxygen ions on p-type Co_3O_4, the hole concentration increased, leading to a decrease in the resistance of the sensor. Upon exposure to H_2S, the gas molecules react with the ionized oxygen species, leading to a decrease in the hole concentration of Co_3O_4. Moreover, the other reason for the high response is the hollow structure of Co_3O_4, which provides large adsorption sites. Besides the above-mentioned two reasons, a p–p heterojunction is formed between Co_3O_4 (p-type) and graphene (p-type), which shifts the band structure of Co_3O_4 and graphene. Thus, electrons get transferred from Co_3O_4 (CB) to graphene (CB) and holes are transferred in the opposite direction (illustrated in Fig. 16b) owing to the formation of a space charge region (SCR). Consequently, a built-in electric field is generated, which promotes more oxygen ions to be chemisorbed and influenced the response of the sensor. Additionally, a high concentration of graphene decreases the effect of the metal oxide given that its sheet structures can cover the oxides. The sensor was tested at various temperatures (illustrated in Fig. 16c) and showed the maximum response at 50 °C.

In another work, Yang *et al.* used NiO–nitrogen-doped rGO as a sensing material for H_2S sensing.[52] After exposure, the analyte gas attached to the pre-adsorbed oxygen, which was confirmed *via* XPS, where the concentration of pre-adsorbed oxygen decreased by up to ~84% due to the redox reaction between the oxygen ions and H_2S gas.

$$H_2S(gas) \rightarrow H_2S(ads) \quad (18)$$

$$2H_2S(ads) + 3O_2^-(ads) \rightarrow 2SO_2(ads) + 2H_2O + 3e \quad (19)$$

The as-made sensor showed high sensitivity (54.6%) even at 50 °C. Further, NiO–boron–nitrogen-doped rGO was synthesized chemically and used as an H_2S detector.[207] By doping boron and nitrogen, the absorption of oxygen anions increased, which increased the number of adsorption sites for the gas. Moreover, the electronegative boron and electropositive nitrogen were attributed to the localized electrostatic potential given that the B-active sites are beneficial for the easy capture of oxygen anions, whereas the N-active sites are beneficial for converting the surface-adsorbed oxygen into oxygen radicals. Although the sensitivity was not affected much, the LOD was five-times lower than that of the NiO–nitrogen-doped rGO-based sensor.

Recently, Shewale *et al.* fabricated an H_2S gas sensor based on Cu-doped ZnO decorated with rGO nanosheets at ambient temperature.[206] The response of the as-made sensor depends on the defected sites, SCR, and formation of a p–n junction between the metallic rGO and semiconducting Cu-doped ZnO, where the electrons transfer from rGO to Cu-doped ZnO. Upon exposure to the analyte gas, the H_2S molecules get adsorbed on the surface of the sensor, and the interaction occurs between the pre-chemisorbed oxygen molecules and H_2S gas-discharged free electrons, which neutralize the holes in rGO, and therefore reduce the size of the charge conduction channels, leading to an increase in the width of the SCR, further increasing the response of the sensor. Additionally, sensing affects the Schottky barrier height and contributes to the performance of the sensor. This sensor detected H_2S molecules (150 ppm) within 12 s, which decreased with an increase in concentration. The noise of the sensor (0.0208) and detection limit (136 ppb) were calculated as follows:

$$RMS_{noise} = \sqrt{\frac{S^2}{N}} \quad (20)$$

$$DL = 3\frac{RMS_{noise}}{Slope} \quad (21)$$

A very small change in the response of the sensor (5%) was observed after 35 days. Moreover, the selectivity of the sensor was confirmed by its lower sensitivity towards H_2 gas. Table 8 summarizes a few recent works on CNM hybrid nanocomposites as H_2S sensors.

According to Table 8, it can be seen that CNTs are less explored than graphene derivatives (rGO) for H_2S sensing. The reason for this may be that together with high sensitivity, rGO hybrid composites show very small LOD values.

4.7 Volatile organic compound sensors

The vapours of numerous volatile organic compounds (VOCs) such as ethanol (C_2H_5OH), toluene (C_7H_8), liquid petroleum gas (LPG), triethylamine (TEA), formaldehyde (HCHO), and acetone are another class of gases that should be sensed given that their presence can be harmful. Moreover, various VOCs are exhaled during breathing. Thus, the detection of these exhaled VOCs can help in the prediction of several physiological conditions in the human body.[215] Consequently, it may be possible to diagnose cancer and other diseases.

4.7.1 Sensing with CNTs and their hybrid nanocomposites. Sensors fabricated using modified CNTs have also been used for sensing various VOCs such as ethanol,[216,217] LPG,[218] acetone,[219,220] formaldehyde,[221,222] toluene and trinitrotoluene.[223] Several VOC-based sensors are presented in this section.

Recently, Guo *et al.* fabricated an ethanol sensor having functionalized CNT-decorated $ZnSnO_3$ (hollow box), which was synthesized *via* the hydrothermal technique.[216] While sensing ethanol vapors, CO_2 and H_2O gases are produced after the interaction of the analyte molecules with the pre-adsorbed oxygen ions, and the corresponding series of reactions occur as follows:

$$e + O_{2(abs)} \rightarrow O_2^- \quad (22)$$

$$2e + O_{2(abs)} \rightarrow 2O^- \quad (23)$$

$$C_2H_5OH + 3O_2^- \rightarrow 2CO_2 + 3H_2O + 3e \quad (24)$$

Table 8 Comparative study of the parameters for significant works done on H_2S sensing using CNM hybrid nanocomposite sensors

Sensing material	Analyte	Operating temperature	Response	Response time	Recovery time	Limit of detection	Reference
Fe_2O_3-SWCNTs	100 ppm H_2S	RT	18.3%[b]	—	—	—	Hua *et al.* (2017)[107]
CNTs-SnO_2-CuO	40 ppm H_2S	RT	19%[c]	240 s	600 s	10 ppm	Zhao *et al.* (2020)[81]
3 wt% CNTs-doped CuO–SnO_2	0.1 ppm H_2S	40 °C	4.441[a]	8.3 s	11.5 s	—	Fan *et al.* (2019)[208]
SnO_2-rGO	4 ppm NO_2	200 °C	185[a]	8 s	215 s	0.5 ppm	Bhangere *et al.* (2020)[101]
	40 ppm H_2S		3.7[a]	240 s	1240 s	2 ppm	
Co_3O_4-4.6 wt% rGO	50 ppm H_2S	50 °C	30.6[a]	—	170 s	0.1 ppm	Liu *et al.* (2019)[205]
	100 ppm H_2S		62.13[a]				
NiO–(boron–nitrogen-doped rGO)	20 ppm H_2S	150 °C	16.6[a]	38 s	44 s	24 ppb	Shanmugasundaram *et al.* (2019)[207]
	50 ppm H_2S	35 °C	1.85[a]	28 s	75 s		
	100 ppm H_2S	50 °C	5.84[a]	29 s	78 s		
	100 ppm H_2S	100 °C	~82[a]				
Cu-doped ZnO-rGO	100 ppm H_2S	24 °C	0.87%[b]	14 s	32 s	136 ppb	Shewale *et al.* (2020)[206]
CuO-rGO	5 ppm H_2S	100 °C	~28[a]	20 s	920 s	—	Yin *et al.* (2019)[209]
Cu_2O-rGO	1 ppm H_2S	40 °C	20%[b]	—	—	—	Zhou *et al.* (2019)[210]
Au–SnO_2-rGO	50 ppm SOF_2	110 °C	15.9%[b]	41 s	68 s	—	Zhang *et al.* (2019)[211]
	50 ppm H_2S		−14.8%[b]	26 s	35 s		
GrQD–SnO_2/ZnO	0.1 ppm H_2S	RT	15.9[a]	14 s	13 s	—	Shao *et al.* (2020)[212]
1.0 wt% rGO-loaded $ZnFe_2O_4$ NFs	1 ppm H_2S	350 °C	147[a]	<10 s	~500 s	0.14 ppb	Hoang *et al.* (2019)[213]
		450 °C		<10 s	~130 s		
SnO2-rGO	100 ppm H_2S	125 °C	33.025%[b]	209 s	900 s	42 ppb	Chu *et al.* (2018)[214]
	10 ppm SOF_2		−0.324%[b]	255 s	330 s	510 ppb	
NiO–nitrogen-doped rGO	50 ppm H_2S	50 °C	24.96[a]		12 s	100 ppb	Yang *et al.* (2017)[52]
	100 ppm H_2S	92 °C	31.95[a]		36 s		
	10 ppm H_2S	133 °C	8.42[a]		197 s		
	0.1 ppm H_2S	92 °C	54.06[a]				
		92 °C	~10.5[a]				
		92 °C	1.6[a]				

[a] R_a/R_g (oxidizing gas) or R_g/R_a (reducing gas). [b] $\Delta R/R_a$. [c] $\Delta R/\Delta C$.

$$C_2H_5OH + 6O^- \rightarrow 2CO_2 + 3H_2O + 6e \quad (25)$$

As shown in Fig. 17a, the released electrons are delivered to $ZnSnO_3$, and consequently decrease the DL thickness. Together with $ZnSnO_3$, CNTs also have a great impact on the performance of the sensor given that in air, a p(CNT)–n($ZnSnO_3$) heterojunction is formed, where the electrons transfer from $ZnSnO_3$ to the CNTs due to their different Fermi levels, and after exposure to ethanol, the electrons released back to $ZnSnO_3$. Moreover, the BET surface area of CNT@$ZnSnO_3$ is higher (45.73 $m^2 g^{-1}$) by up to seven-folds that of $ZnSnO_3$. Besides, the dipole–dipole interaction between the COOH groups of the functionalized CNTs and OH group of ethanol enhanced the sensing behaviour of the as-made sensors. However, to check the selectivity, the sensor was exposed to 100 ppm ethanol, acetone, benzene, methylbenzene, formaldehyde, and ammonia at 240 °C and it showed the highest sensitivity towards ethanol (shown in Fig. 17b).

Likewise, CNT-based acetone sensors were also fabricated. In one of the works, Dai *et al.* studied α-Fe_2O_3 nanowires wrapped on MWCNTs (shown in Fig. 18a) for sensing acetone.[224] The basic phenomenon of the absorption of ambient oxygen on the surface of Fe_2O_3 was attributed to the increase in electron concentration. The released electrons from α-Fe_2O_3 were captured by the CNTs, leading to a change in resistance. In addition, when α-Fe_2O_3 and MWCNTs come in contact, p–n heterojunction is formed (having different bandgaps) at the interface of the CNTs and iron oxide (illustrated in Fig. 18b), which promotes the performance of the sensor. Nonetheless, the surface area of α-Fe_2O_3-CNT was higher than that of α-Fe_2O_3. For the investigation of selectivity, the as-made sensor was studied using various types of gases such as methanol, formaldehyde, ethanol, acetone, toluene, and benzene (shown in Fig. 18d). Moreover, Jia *et al.* studied the same sensing material for acetone having a flower-type morphology of iron oxide.[219] The proposed sensing mechanism model is same as described above (illustrated in Fig. 18e), but due to the metal oxide having different structures, the sensing response was affected.

Fig. 18f shows the response curve indicating the response and recovery time of the α-Fe_2O_3 (3.4 s/10.6 s) and α-Fe_2O_3-MWCNTs (2.3 s/10.6 s) sensors. Further for LPG sensing, a PANI-CNT-V_2O_5 hybrid nanocomposite was studied as a sensing material.[225] When the sensing material is exposed to LPG, the analyte molecules are adsorbed on CNT-V_2O_5 and the adsorbed molecules are oxidized due to the transfer of electrons from PANI owing to the increase in resistance. The sensor showed a small LOD value (10 ppm). Recently, Reddy *et al.* studied a CeO_2 nano-hexagon-decorated rGO/CNT heterostructure for LPG sensing.[226] After exposure, the chemisorbed

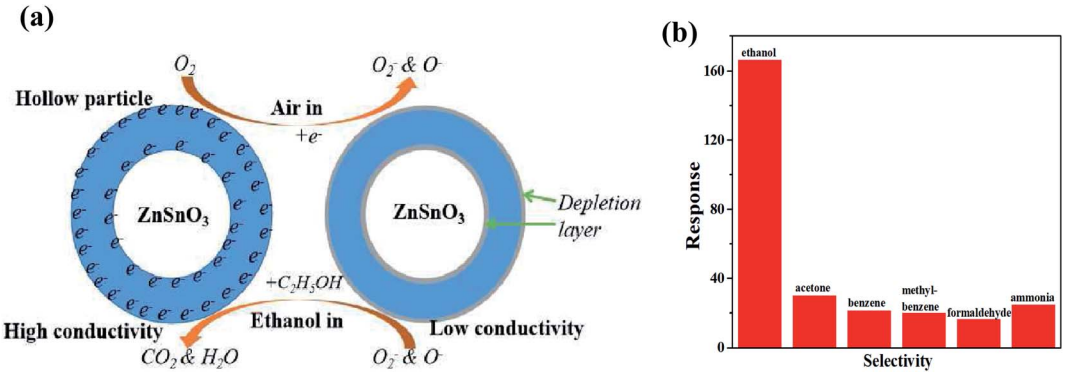

Fig. 17 (a) Ethanol sensing mechanism of $ZnSnO_3$ hollow particles. (b) Sensing response (R_a/R_g) of CNT@$ZnSnO_3$ exposed to different types of gases, *i.e.* ethanol, acetone, benzene, methyl-1-benzene, formaldehyde and ammonia (from left to right)[216] (reprinted from ref. 216, Copyright (2020), with permission from Elsevier).

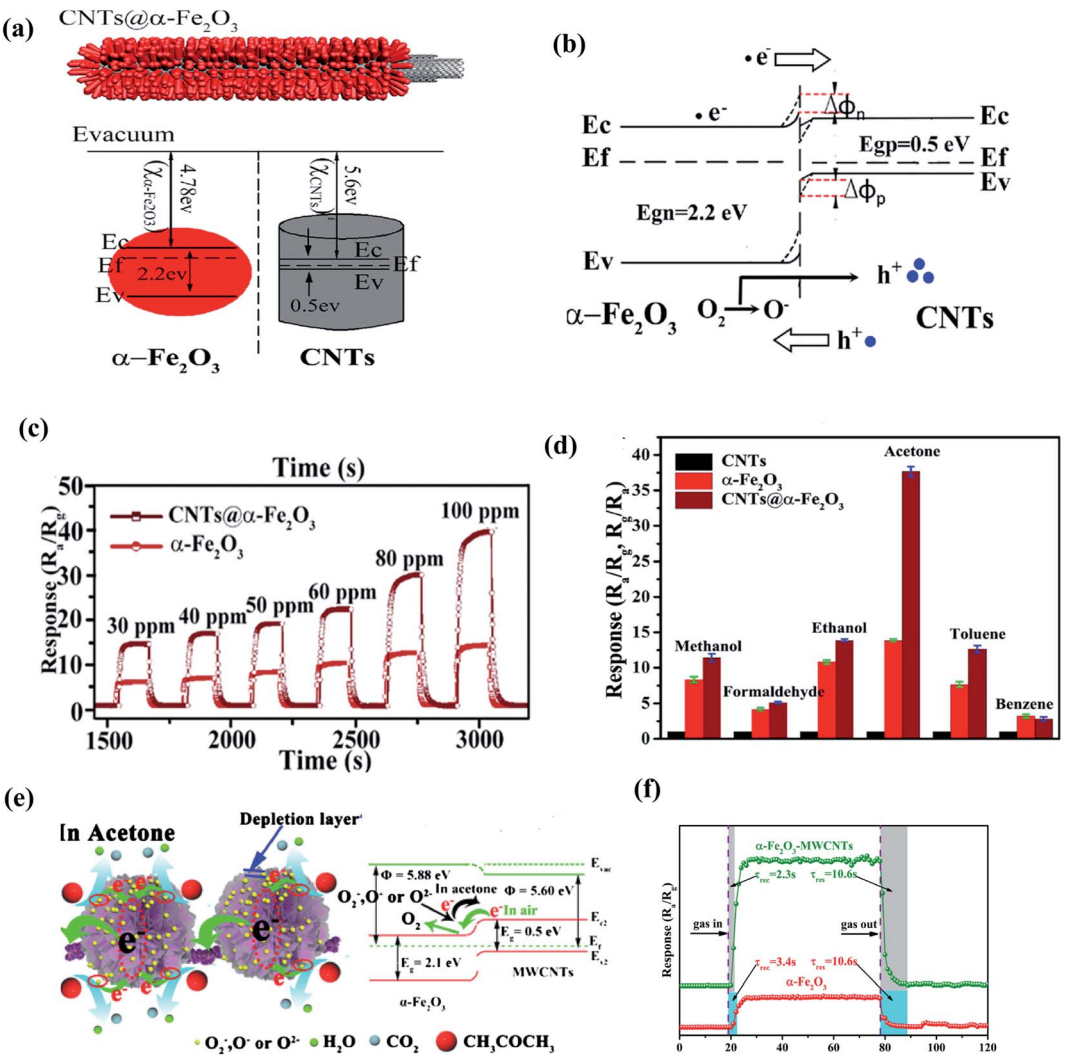

Fig. 18 (a) Qualitative band diagrams of α-Fe_2O_3 and CNTs, (b) energy band structure of the CNTs@α-Fe_2O_3 heterostructure in air, (c) resistance curves of pure α-Fe_2O_3 and α-Fe_2O_3-MWCNTs towards varying concentrations of acetone (30–100 ppm) at 225°, (d) response curve towards various organic compounds[224] (adapted with permission from ref. 224. Copyright (2017) American Chemical Society), and (e) Schematic of the gas sensing mechanism of α-Fe_2O_3-MWCNT nanocomposites. (f) response curve of pure α-Fe_2O_3 and α-Fe_2O_3-MWCNTs towards 50 ppm acetone at 220 °C.[219] (Reprinted from ref. 219, Copyright (2017), with permission from Elsevier).

oxygen ions oxidized the LPG reducing gas molecules and released electrons to CeO_2-rGO/CNT and increased the conductivity. Moreover, rGO and CNTs provided abundant adsorption sites for atmospheric oxygen, thus resulting in a high sensing response. During LPG sensing, a series of reactions occurs as follows:

$$C_nH_{2n+2} + O_2^- \leftrightarrow C_nH_{2n}{:}\,O_{(gas)} + e + H_2O \rightarrow CO_2(gas) + H_2O \quad (26)$$

$$C_4H_{10} + 13/2O_2^- \leftrightarrow 4CO_2(gas) + 5H_2O + 13/2e \quad (27)$$

$$C_3H_8 + 5O_2^- \leftrightarrow 3CO_2(gas) + 4H_2O + 5e \quad (28)$$

where $n = 1, 2, 3$ and 4, indicating different organic compounds such as CH_4, C_3H_8, and C_4H_{10}. The sensor showed the highest sensitivity (42%) at 400 ppm LPG at room temperature, which is 1.5, 1.9 and 2.2 times that of CeO_2/rGO, CeO_2/CNT, and CeO_2 respectively.

In another work, Septiani *et al.* sensed toluene vapours using an MWCNT-ZnO-based sensor.[227] During sensing, the analyte gas came in contact with oxygen ions and released electrons, which reduced the resistance of the sensor. Moreover, when the analyte gas contacted the sensor, the barrier height decreased and the resistance of the sensor decreased. Also, the formation of a heterojunction also helped to improve the sensing performance.

4.7.2 Sensing with graphene and its hybrid nanocomposites. Similar to CNTs, graphene-based nanocomposites are also promising candidates for sensing not only pollutants and explosive gases, but also several VOCs[15,228] such as TEA,[85,229] toluene,[230] formaldehyde,[231–233] and LPG.[234]

Recently, Yuan *et al.* sensed TEA using a double-layer Co_3O_4 coated on rGO (D-Co_3O_4/rGO)-based sensor.[228] The adsorption of oxygen anions on Co_3O_4 (p-type) results in the formation of a hole accumulation layer (HAL). When the reducing gas TEA interacts with these chemisorbed oxygen ions, the corresponding reaction takes place, as follows:

$$2N(CH_2CH_3) + 13O^- \rightarrow 4CO_2 + N_2 + 5H_2O + 13e \quad (29)$$

The released electrons lead to a decrease in the HAL thickness. Moreover, a p–p isotherm junction is formed between rGO and Co_3O_4, also contributing to the electron transfer, and thus affects the response of the sensor. Besides, the double-layered structure provides a high surface area for the adsorption of more analyte molecules (illustrated in Fig. 19a).

Likewise, Peng *et al.* synthesized boron-doped graphene coated with Au@SnO_2 composite for TEA sensing.[235] The presence of Au NPs promotes the adsorption of oxygen ions, resulting in a wider EDR at the Au@SnO_2 interface, which influences the overall sensor response (illustrated in Fig. 19b). In addition, more adsorption sites are provided by Au NPs. The as-designed sensor showed a high response (~69%) for 1 ppm TEA.

Wei *et al.* doped 1 wt% rGO in α-Fe_2O_3 to improve the sensing performance for TEA.[236] When exposed to air, α-Fe_2O_3 donates electrons to oxygen, forming an EDL, whose width decreases *via* gas adsorption. In addition, rGO is another crucial factor for improved sensing *via* the formation of a p–n

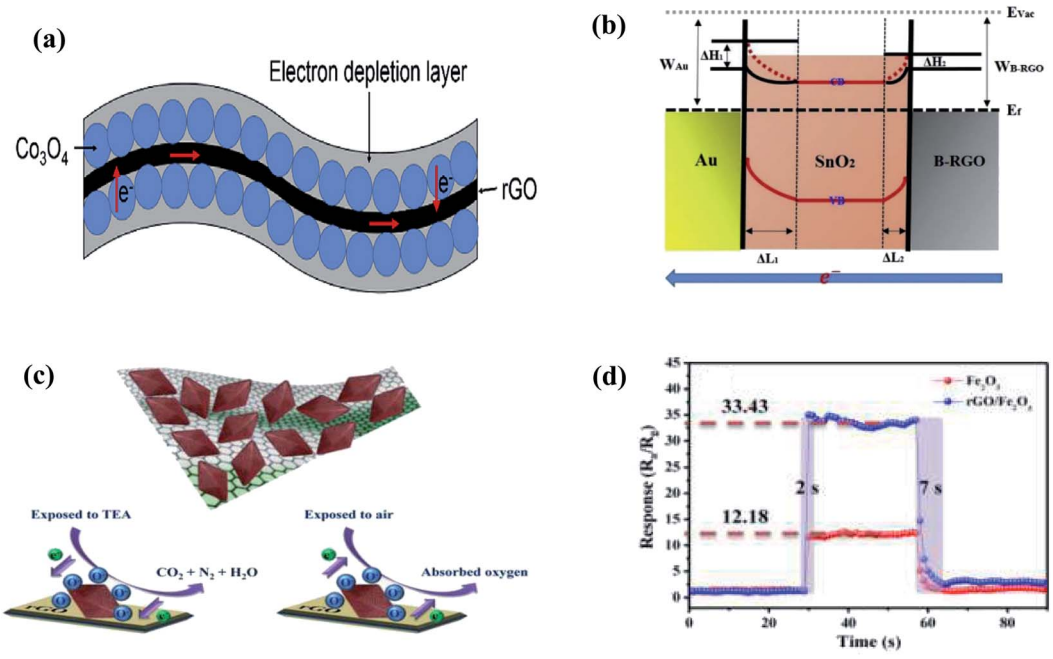

Fig. 19 (a) Schematic of the sensing mechanism of D-Co_3O_4/rGO composite[228] (reprinted from ref. 228.,Copyright (2019), with permission from Elsevier). (b) Energy band diagram of the B-rGO/SnO_2@Au heterostructure sensor[235] (reprinted from ref. 235, Copyright (2020), with permission from Elsevier). (c) Schematic diagram of the possible gas sensing mechanisms of rGO/α-Fe_2O_3 nanocomposite. (d) Dynamic response–recovery curve (100 ppm TEA) of pure α-Fe_2O_3 spindles and rGO/α-Fe_2O_3 nanocomposite at 280 °C (ref. 236) (reprinted from ref. 236, Copyright (2017), with permission from Elsevier).

heterojunction at the interface of α-Fe_2O_3 and rGO. Fig. 19c describes the mechanism for TEA sensing. The hybrid sensor showed 2.7-times higher sensitivity at 280 °C. The response–recovery curves of the pure α-Fe_2O_3 spindles and rGO/α-Fe_2O_3 nanocomposite at 280 °C are illustrated in Fig. 19d.

Moreover, Seekaew *et al.* (2019) fabricated a toluene (C_7H_8) gas sensor based on a graphene–CNT hybrid nanostructure decorated with TiO_2,[237] where a Schottky metal-semiconductor junction is formed between G/CNT NS-TiO_2. Upon exposure, the C_7H_8 vapors interact with the pre-absorbed oxygen ions according to the following reaction:

$$C_7H_8(gas) + 9O^-(ads) \rightarrow 7CO_2(gas) + 4H_2O(gas) + 9e \quad (30)$$

The released electrons move to TiO_2, which further increase the barrier height (illustrated in Fig. 20b), and consequently increase the resistance of the sensor. The as-made sensor showed a higher response than CNT-decorated TiO_2 given that the TiO_2 NPs were well dispersed on the CNTs grown on graphene because they were agglomerated.

Similar to other organic compounds, LPG vapors are also detected using graphene-based sensors.[239] In one study, Goutham and coworkers synthesized a CdO-doped graphene nanocomposite for LPG sensing.[240] In LPG sensing, the gas molecules interact with the pre-absorbed oxygen ions on the surface of the sensor, producing CO_2, H_2O, and electrons.

In addition to other compounds, HCHO vapors are also detected using graphene-based sensors.[241] In this field, Wang *et al.* used graphene oxide *in situ* SnO_2 sheets as a sensing material for the detection of formaldehyde (shown in Fig. 20c). A Schottky junction is formed between GO and SnO_2, and the electrons transfer from SnO_2 to GO, thus decreasing the resistance of the sensor. Moreover, GO helps to decrease the agglomeration of the SnO_2 NPs. Accordingly, it increases the

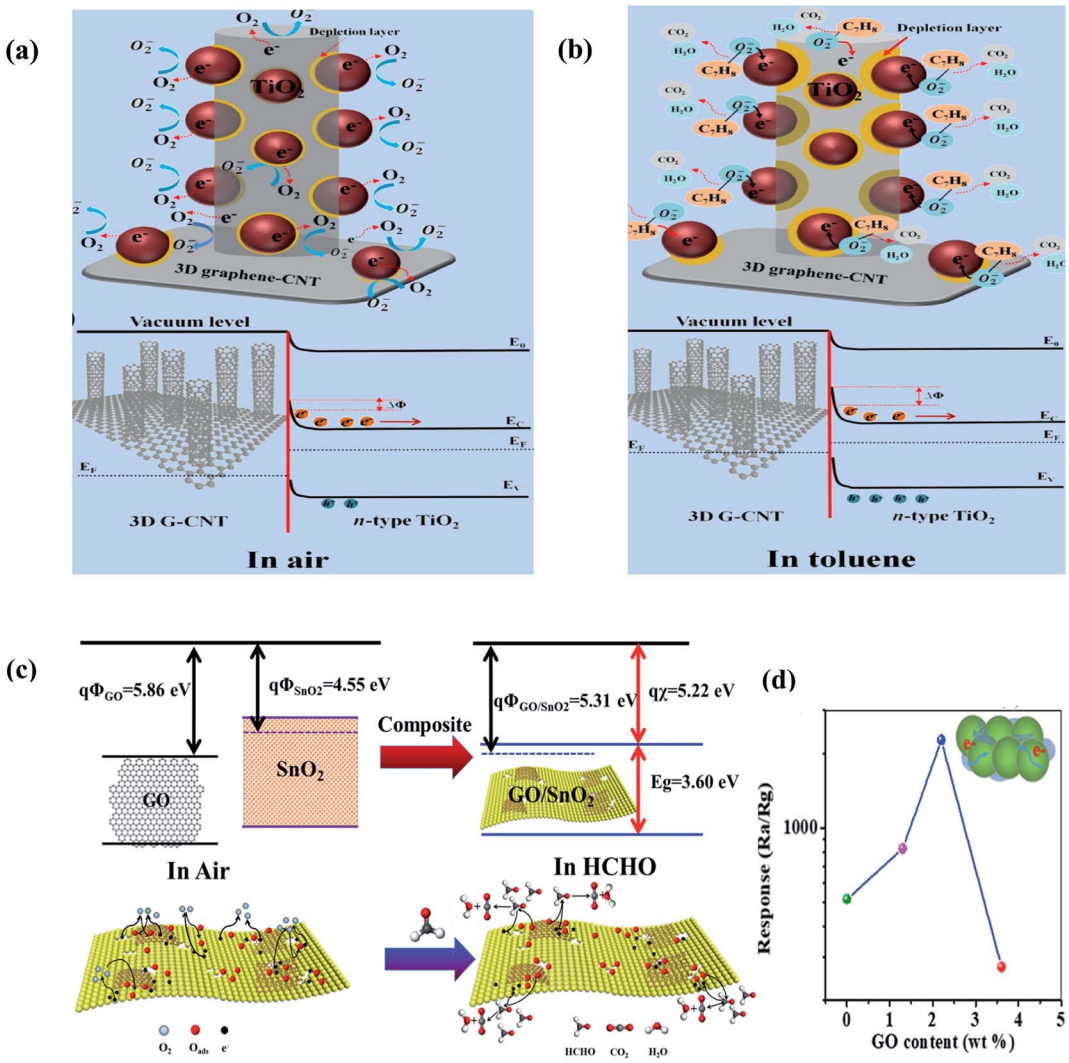

Fig. 20 Schematic and energy band diagrams of 3D TiO_2/G-CNT gas sensors in (a) air and (b) toluene[237] (reprinted from ref. 237, Copyright (2019), with permission from Elsevier). (c) Schematic description of formaldehyde sensing mechanism on GO/SnO_2. (d) Relation between response *vs.* GO content for GO/SnO_2 NS-T (T = 450 °C, 475 °C, 500 °C, and 525 °C) operated at 60 °C (ref. 238) (reprinted with permission from ref. 238. Copyright (2017) American Chemical Society).

available adsorption sites for a high sensor response. When HCHO (electron donor) interacts with the sensing material, the following reaction takes place:

$$HCHO(g) + O^-/O_2^-(ads) \rightarrow HCOOH(g) + e \quad (31)$$

$$HCHO(g) + O^-/O_2^-(ads) \rightarrow CO_2(g) + H_2O(g) + e \quad (32)$$

Beyond 2.2 wt% GO in the sensor, the response of the sensor started to decrease (shown in Fig. 20b) due to the poor dispersion of the sheets.

Besides the above-mentioned volatile compounds, several other VOCs such as DMMP[242] and ethanol[243] have also been sensed using graphene hybrid nanocomposite sensors. Table 9 summarizes the recent works on CNM hybrid nanocomposites towards various VOCs.

As shown in Table 9, various VOCs were detected using CNM hybrid nanocomposite-based sensors. However, there are diverse compounds (>400) exhaled during breathing, which can help to predict typhoid, lung cancer, breast cancer, asthma, kidney malfunctioning, *etc.* Therefore, more research should be performed on CNM hybrid nanocomposites for the detection of VOCs.

As mentioned in Section 4, CNMs-based composites show high sensitivity towards various gases but atmospheric moisture is also one of the major concern which is described in next section.

5. Effect of atmospheric moisture

It has been reported that environmental humidity can limit the real-life applications of CNMs-based gas sensors, where it has positive or negative effects, depending on various factors such as the type of gas that should be sensed, its concentration and the operating temperature of the sensor. When moisture interacts with CNT-based sensors, electrons migrate from H_2O to CNT, which can convert p-type CNTs to n-type CNTs. In this case, Zhang *et al.* synthesized an SWCNT-based composite as a gas sensor, which had a negligible effect from moisture.[247] According to the reported mechanism, PANI (negative response to relative humidity (RH)) and SWCNTs (positive response to RH) balanced the humidity affect.

Moreover, in terms of pristine graphene (hydrophilic), moisture or water molecules adsorb on its surface, and consequently block its active sites. The other class of graphene, GO, has many functional groups on its surface, which can form hydrogen bonds between moisture molecules and its oxygenated functional groups, and therefore can endure the sensing performance towards humidity. Specifically, due to the hydrophilic nature of GO, H_2O molecules get adsorbed and can form a molecularly thin layer on its surface, which is attributed to the high adsorption of gas, where the layer thickness can be enhanced with RH. Wu *et al.* concluded that a GO-based sensor had a three times larger value at 70% RH towards 1 ppm NO_2.[37] Further Khurshid *et al.* reported similar humidity effects for NH_3 gas. Upon the interaction of NH_3 with moisture, the water molecules act as an electron acceptor.[48]

Although humidity has a positive effect on GO-based sensors, the response of the sensor declines with respect to moisture. Accordingly, rGO has better immunity to RH given that it is hydrophobic in nature, and thus rGO-based sensors are less impaired by humidity. Due to this unique feature, rGO-based composites has little impact from RH.

Table 9 Comparative study of the parameters for significant works done on VOC sensing using CNM hybrid nanocomposite sensors

Sensing material	Analyte	Operating temperature	Response	Response time	Recovery time	Limit of detection	Reference
α-Fe_2O_3-MWCNTs	50 ppm C_3H_6O	220 °C	20.32[a]	2.3 s	10.6 s	—	Jia *et al.* (2019)[219]
CNTs-$ZnSnO_3$	100 ppm C_2H_5OH	240 °C	166[a]	6 s	—	—	Guo *et al.* (2020)[216]
CNT-rGO decorated with Co_3O_4	50 ppm C_2H_5OH	RT	1.36%[b]	—	—	—	Morsy *et al.* (2019)[244]
CNT-V_2O_5 polymerized with PANI	50 ppm LPG	30 °C	300%[b]	20 s	15 s	—	Albaris *et al.* (2019)[225]
CeO_2-decorated rGO-CNT	400 ppm LPG	RT	42%[b]	26 s	98 s	—	Reddy *et al.* (2020)[226]
CNTs decorated *via* Fe_2O_3	5 vol% LPG	RT	—	10 s	59 s	—	Chaitongrat *et al.* (2019)[72]
ZnO NRs-MWCNTs	100 ppm C_2H_5OH	370 °C	26.1[a]	2 s	16 s	—	Cao *et al.* (2018)[245]
CNTs coated *via* Au NPs	800 ppm propanone	RT	2.98%[b]	—	—	—	Lam *et al.* (2019)[246]
Boron-doped Gr coated Au–SnO_2	1 ppm TEA	100 °C	69.1%[b]	27 s		100 ppb	Peng *et al.* (2020)[235]
Fe_2O_3-rGO	50 ppm TEA	280 °C	24%[a]	2 s	7 s	—	Wei *et al.* (2020)[236]
Double layer Co_3O_4/rGO	100 ppm TEA	200 °C	~25[a]	30 s	32 s	—	Yuan *et al.* (2019)[228]
12 layered r (GO/rGO)	50 ppm DMMP	RT	8.95%[b]	4 min	3 min	—	Wang *et al.* (2019)[242]
TiO_2-Gr-CNT hybrid	500 ppm toluene vapors	RT	42.9%[a]	9 s	11 s	—	Seekaew *et al.* (2019)[237]
rGO-Au	50 ppm LPG	RT	22.5[a]	~5 s	~35 s	50 ppm	Taheri *et al.* (2018)[239]
SnO_2-GO	100 ppm HCHO	60 °C	2275.7[a]	81.3 s	33.7 s	—	Wang *et al.* (2019)[238]
HA-HCl-rGO	16 ppm HCHO	RT	75%[b]			0.023 ppm	Zhou *et al.* (2020)[241]
Pd–SnO_2-Gr	2% C_2H_5OH	200 °C	14.8%[b]	~15 s	~12.5 s	—	Dhall *et al.* (2018)[243]

[a] R_a/R_g (oxidizing gas) or R_g/R_a (reducing gas). [b] $\Delta R/R_a$.

In addition, the effects of humidity on CNMs-based gas sensors is affected by a variation in temperature. Wu *et al.* showed that by increasing the temperature, the humidity effect can be nullified.[37] Further, the concentration of gas analytes can also influence the moisture effect. In this context, Tang *et al.* fabricated an NH_3 sensor using ppy/rGO as the sensing material and studied the effect of moisture towards 1 ppm to 4 ppm NH_3.[248] Although CNMs-based sensors have the ability to avoid moisture, still a lot of work is required for their applications in the field.

Besides humidity effects, many other problems of CNMs-based sensors are discussed in Section 6.

6. Current challenges

Although nanocarbon-based sensors have high sensitivity, more efforts are required for their profit-oriented establishment given that they have many challenges such as low reproducibility,[16] cross-sensitivity,[249] non-uniform dispersion,[12] irreversible recovery,[95] low stability of functional groups, and defects.[250] Furthermore, besides the expensive and complex synthesis of CNMs, they require sophisticated handling during device fabrication and sensing,[251] for example, it is difficult to control the layers of graphene, its degree of functionality and walls of CNTs with a particular chiral family. In the case of graphene synthesized *via* CVD, transferring the graphene sheet is also a challenge.[252] Together with these challenges, the other dire challenge is cross-sensitivity given that the sensing environment having a mixture of gases with similar structures and belonging to the same family may interfere with the response of the sensor. Therefore, the major challenge is that pristine CNMs show low sensitivity and selectivity,[181,253] which can be resolved by functionalizing them either with metal oxides or functional groups, *i.e.* carboxylic and ketone groups. Furthermore, for an ideal sensor, its LOD should be low to sense a very small concentration of gases. By using aligned sensing structures, the LOD can be reduced. Moreover, flexible sensors are in a high demand, which researchers are working on nowadays.[20] In this case, various polymers incorporated with CNTs and graphene, GO and rGO have been explored without ruining their sensitivity. Moreover, for medical diagnosis applications, less toxic sensors are of great importance, but CNMs have a high toxic effect on the human body,[20,254] and thus researchers are working on introducing the less toxic GrQDs (0-D) as a new sensing material, but a lot of work has to be performed. To date, most of the research on CNM chemiresistive sensors is based on lab-scale tests. Hence, for industrialization, the large-scale production of CNMs such as graphene and CNTs is also a major concern.

7. Conclusion

In the past two decades, the progress and application of carbon nanomaterials (CNMs)-based chemiresistive sensor technology have been increasing at a considerable rate due to the inherent morphology and properties of CNMs. CNMs such as CNTs, graphene and their derivatives have abundant adsorption sites, tunable electrical properties, low density, high carrier mobility, low operating temperature, long lifetime, and easy recovery, which make them suitable alternatives to the standard MOS chemiresistive sensors towards various toxic pollutant gases, explosive gases, and volatile compounds. Theoretically and experimentally, it has been established that the electrical resistance and local density of states of CNMs can be reversibly changed upon exposure to certain vapours.

According to the latest trend in chemiresistive sensor application, it was found that numerous studies related to CNMs and their hybrid nanocomposites are considered ideal sensing materials. Due to the presence of a higher surface area, planar structure, better bending ability, low electrical noise, easy functionalization, and high availability of adsorption sites, graphene is the most preferable candidate as a gas sensing material. However, pristine graphene has some drawbacks such as lack of functional groups, difficult synthesis and handling process, and thus its derivatives have also been studied as sensing materials. Among the graphene derivatives, rGO has the highest sensitivity due to its high charge mobility and presence of vacancies, which are created *via* the removal of oxygen groups. Similarly, other CNMs such as CNTs have also been explored for gas sensing applications. Although graphene-based sensors show better sensitivity, CNTs still have some advantages over them. In the case of CNTs, MWCNTs are favoured due to their easy synthesis, whereas SWCNTs possess high repeatability. Nevertheless, for a wide range of gas sensing, higher selectivity, higher response and good flexibility, various nanostructures such as chalcogenides, metallic nanoparticles, metal oxides and polymers are incorporated in these CNMs. These composite-based smart sensors are highly active towards several harmful and toxic gases, which are greatly adopted in the research field for industrial applications and summarized herein. The future of CNMs-based hybrid sensors is undoubtedly very bright given that these sensors outperform the commercialized MOS sensors because the commercialized sensors are bulky and have high operating temperatures due to the chemisorption of analytes molecules. This new class of sensors can show superior sensitivity and selectivity, which can be used in a plethora of applications.

Conflicts of interest

The author assures that this manuscript has not been submitted elsewhere for publication and all authors have been informed. We declare no conflict of interest.

Acknowledgements

Authors are highly grateful to Director, CSIR-NPL for his kind permission to write a review article and publish the same. The author would like to acknowledge the Department of Science and Technology for SRF fellowship.

References

1 H. Li, J. Zhang, G. Li, F. Tan, R. Liu, R. Li, T. Zhang, H. Jin and Q. Li, *Carbon*, 2014, **66**, 369–376.

2 L. Sacco, S. Forel, I. Florea and C.-S. Cojocaru, *Carbon*, 2020, **157**, 631–639.
3 Z. Hou, J. Wu, W. Zhou, X. Wei, D. Xu, Y. Zhang and B. Cai, *IEEE Trans. Electron Devices*, 2007, **54**, 1545–1548.
4 R. Malik, V. K. Tomer, Y. K. Mishra and L. Lin, *Appl. Phys. Rev.*, 2020, **7**, 021301.
5 C. Wang, C. Feng, M. Wang, X. Li, P. Cheng, H. Zhang, Y. Sun, P. Sun and G. Lu, *RSC Adv.*, 2015, **5**, 29698–29703.
6 A. Maity and S. Majumder, *Sens. Actuators, B*, 2015, **206**, 423–429.
7 R. Kumar, X. Liu, J. Zhang and M. Kumar, *Nano-Micro Lett.*, 2020, **12**, 1–37.
8 P.-G. Su and J.-H. Yu, *Sens. Actuators, A*, 2020, **303**, 111718.
9 S. W. Lee, W. Lee, Y. Hong, G. Lee and D. S. Yoon, *Sens. Actuators, B*, 2018, **255**, 1788–1804.
10 K. Xu, C. Fu, Z. Gao, F. Wei, Y. Ying, C. Xu and G. Fu, *Instrum. Sci. Technol.*, 2018, **46**, 115–145.
11 Y. Wang and J. T. Yeow, *J. Sens.*, 2009, **2009**, 1–24.
12 K. Toda, R. Furue and S. Hayami, *Anal. Chim. Acta*, 2015, **878**, 43–53.
13 K. M. Tripathi, T. Kim, D. Losic and T. T. Tung, *Carbon*, 2016, **110**, 97–129.
14 J. E. Ellis and A. Star, *ChemPlusChem*, 2016, **81**, 1248.
15 T. T. Tung, M. T. Tran, J.-F. Feller, M. Castro, T. Van Ngo, K. Hassan, M. J. Nine and D. Losic, *Carbon*, 2020, **159**, 333–344.
16 T. Han, A. Nag, S. C. Mukhopadhyay and Y. Xu, *Sens. Actuators, A*, 2019, **291**, 107–143.
17 S. Z. N. Demon, A. I. Kamisan, N. Abdullah, S. A. M. Noor, O. K. Khim, N. A. M. Kasim, M. Z. A. Yahya, N. A. A. Manaf, A. F. M. Azmi and N. A. Halim, *Sens. Mater.*, 2020, **32**, 759–777.
18 U. Yaqoob, D.-T. Phan, A. I. Uddin and G.-S. Chung, *Sens. Actuators, B*, 2015, **221**, 760–768.
19 J. Wu, Z. Wu, H. Ding, Y. Wei, W. Huang, X. Yang, Z. Li, L. Qiu and X. Wang, *Sens. Actuators, B*, 2020, **305**, 127445.
20 E. Singh, M. Meyyappan and H. S. Nalwa, *ACS Appl. Mater. Interfaces*, 2017, **9**, 34544–34586.
21 M. Sireesha, V. Jagadeesh Babu, A. S. Kranthi Kiran and S. Ramakrishna, *Nanocomposites*, 2018, **4**, 36–57.
22 T. Seesaard, T. Kerdcharoen and C. Wongchoosuk, in *Semiconductor Gas Sensors*, Elsevier, 2020, pp. 185–222.
23 S. Kumar, V. Pavelyev, N. Tripathi, V. Platonov, P. Sharma, R. Ahmad, P. Mishra and A. Khosla, *J. Electrochem. Soc.*, 2020, **167**, 047506.
24 W. Tian, X. Liu and W. Yu, *Appl. Sci.*, 2018, **8**, 1118.
25 H. Cruz-Martínez, H. Rojas-Chávez, F. Montejo-Alvaro, Y. A. Peña-Castañeda, P. T. Matadamas-Ortiz and D. I. Medina, *Sensors*, 2021, **21**, 1992.
26 X. Vilanova, *Sensors*, 2020, **20**(5), 1373.
27 E. Llobet, *Sens. Actuators, B*, 2013, **179**, 32–45.
28 S. Mao, G. Lu and J. Chen, *J. Mater. Chem. A*, 2014, **2**, 5573–5579.
29 R. B. Mathur, B. P. Singh and S. Pande, *Carbon nanomaterials: synthesis, structure, properties and applications*, CRC Press, 2016.
30 T. Lin, X. Lv, S. Li and Q. Wang, *Sensors*, 2017, **17**, 2779.
31 B. Mehrdad-Vahdati, S. Pourhashem, M. Sedghi, Z. Vaezi, B. Shojaedin-Givi, A. Rashidi and H. Naderi-Manesh, *Toxicol. in Vitro*, 2019, **61**, 104649.
32 M. Li, T. Chen, J. J. Gooding and J. Liu, *ACS Sens.*, 2019, **4**, 1732–1748.
33 W. Li, L.-S. Zhang, Q. Wang, Y. Yu, Z. Chen, C.-Y. Cao and W.-G. Song, *J. Mater. Chem.*, 2012, **22**, 15342–15347.
34 G. Deokar, P. Vancsó, R. Arenal, F. Ravaux, J. Casanova-Cháfer, E. Llobet, A. Makarova, D. Vyalikh, C. Struzzi and P. Lambin, *Adv. Mater. Interfaces*, 2017, **4**, 1700801.
35 N. Zheng, S. Yang, H. Xu, Z. Lan, Z. Wang and H. Gu, *Vacuum*, 2020, **171**, 109011.
36 J. Wu, K. Tao, J. Miao and L. K. Norford, *IEEE MEMS*, 2018, 901–904.
37 J. Wu, Z. Wu, H. Ding, Y. Wei, W. Huang, X. Yang, Z. Li, L. Qiu and X. Wang, *ACS Appl. Mater. Interfaces*, 2020, **12**, 2634–2643.
38 A. Zöpfl, M.-M. Lemberger, M. König, G. Ruhl, F.-M. Matysik and T. Hirsch, *Faraday Discuss.*, 2014, **173**, 403–414.
39 C. Lu and H. Chiu, *Chem. Eng. J.*, 2008, **139**, 462–468.
40 M. E. Birch, T. A. Ruda-Eberenz, M. Chai, R. Andrews and R. L. Hatfield, *Ann. Occup. Hyg.*, 2013, **57**, 1148–1166.
41 U. Kumar and B. C. Yadav, *J. Taiwan Inst. Chem. Eng.*, 2019, **96**, 652–663.
42 S. Dash and A. Patnaik, *Microw. Opt. Technol. Lett.*, 2018, **60**, 1183–1187.
43 J. S. Im, S. C. Kang, S.-H. Lee and Y.-S. Lee, *Carbon*, 2010, **48**, 2573–2581.
44 U. K. Sur, *Int. J. Electrochem.*, 2012, **2012**, 237689.
45 M. Kooti, S. Keshtkar, M. Askarieh and A. Rashidi, *Sens. Actuators, B*, 2019, **281**, 96–106.
46 M. G. Stanford, K. Yang, Y. Chyan, C. Kittrell and J. M. Tour, *ACS Nano*, 2019, **13**, 3474–3482.
47 S. Zhang, H. Wang, J. Liu and C. Bao, *Mater. Lett.*, 2020, **261**, 127098.
48 F. Khurshid, M. Jeyavelan, T. Hussain, M. S. L. Hudson and S. Nagarajan, *Mater. Chem. Phys.*, 2020, **242**, 122485.
49 A. Mikhraliieva, V. Zaitsev, O. Tkachenko, M. Nazarkovsky and E. V. Benvenutti, 2020, arXiv preprint arXiv:2006.05634.
50 N. H. Ha, D. D. Thinh, N. T. Huong, N. H. Phuong, P. D. Thach and H. S. Hong, *Appl. Surf. Sci.*, 2018, **434**, 1048–1054.
51 D. Liu, C. Fu, N. Zhang, H. Zhou and Y. Kuang, *Electrochim. Acta*, 2016, **213**, 291–297.
52 M. Yang, X. Zhang, X. Cheng, Y. Xu, S. Gao, H. Zhao and L. Huo, *ACS Appl. Mater. Interfaces*, 2017, **9**, 26293–26303.
53 J. Huang, X. Yang, S.-C. Her and Y.-M. Liang, *Sensors*, 2019, **19**, 317.
54 J.-H. Cha, S.-J. Choi, S. Yu and I.-D. Kim, *J. Mater. Chem. A*, 2017, **5**, 8725–8732.
55 S. Fasbender, L. Zimmermann, R.-P. Cadeddu, M. Luysberg, B. Moll, C. Janiak, T. Heinzel and R. Haas, *Sci. Rep.*, 2019, **9**, 1–13.
56 S. Kumar, M. Mittal, I. Kaur, K. Dharamvir, B. D. Pant and L. M. Bharadwaj, *Eur. Phys. J.: Appl. Phys.*, 2013, **64**, 20401.

57 N. Janudin, N. Abdullah, W. M. Z. Wan Yunus, F. M. Yasin, M. H. Yaacob, N. Mohamad Saidi and N. A. Mohd Kasim, *J. Nanotechnol.*, 2018, **2018**, 2107898.
58 P. Slobodian, P. Riha, A. Lengalova, P. Svoboda and P. Saha, *Carbon*, 2011, **49**, 2499–2507.
59 C. Cao, C. Hu, L. Fang, S. Wang, Y. Tian and C. Pan, *J. Nanomater.*, 2011, 2011.
60 K. Jirakittidul, N. Vittayakorn, R. Manrean, N. Pornteeranawapat and S. Neamyooyong, *Mater. Res. Express*, 2019, **6**, 115003.
61 M. Zhao, L. Yan, X. Zhang, L. Xu, Z. Song, P. Chen, F. Dong and W. Chu, *J. Mater. Chem. C*, 2017, **5**, 1113–1120.
62 M. Chen, L. Zou, Z. Zhang, J. Shen, D. Li, Q. Zong, G. Gao, G. Wu and Z. Zhang, *Carbon*, 2018, **130**, 281–287.
63 A. N. Naje, R. R. Ibraheem and F. T. Ibrahim, *Photonic Sens.*, 2016, **6**, 153–157.
64 S. Barthwal, B. Singh and N. B. Singh, *Mater. Today: Proc.*, 2018, **5**, 15439–15444.
65 Y. J. Kwon, A. Mirzaei, S. Y. Kang, M. S. Choi, J. H. Bang, S. S. Kim and H. W. Kim, *Appl. Surf. Sci.*, 2017, **413**, 242–252.
66 D. Kumar, P. Chaturvedi, P. Saho, P. Jha, A. Chouksey, M. Lal, J. Rawat, R. Tandon and P. Chaudhury, *Sens. Actuators, B*, 2017, **240**, 1134–1140.
67 A. K. Sharma, A. Mahajan, R. Bedi, S. Kumar, A. Debnath and D. Aswal, *Appl. Surf. Sci.*, 2018, **427**, 202–209.
68 A. K. Sharma, A. Mahajan, R. Saini, R. Bedi, S. Kumar, A. Debnath and D. Aswal, *Sens. Actuators, B*, 2018, **255**, 87–99.
69 N. D. Hoang, V. Van Cat, M. H. Nam, V. N. Phan, A. T. Le and N. Van Quy, *Sens. Actuators, A*, 2019, **295**, 696–702.
70 N. Donato, M. Latino and G. Neri, *Carbon Nanotubes: Res. Appl.*, 2011, **14**, 229–242.
71 P. Dariyal, A. K. Arya, B. Singh and S. Dhakate, *J. Mater. Sci.*, 2020, 1–29.
72 B. Chaitongrat and S. Chaisitsak, *Mater. Sci. Forum*, 2019, **947**, 47–51.
73 U. Kumar and B. Yadav, *J. Taiwan Inst. Chem. Eng.*, 2019, **96**, 652–663.
74 S. S. Varghese, S. Lonkar, K. Singh, S. Swaminathan and A. Abdala, *Sens. Actuators, B*, 2015, **218**, 160–183.
75 J. E. Proctor, D. M. Armada and A. Vijayaraghavan, *An introduction to graphene and carbon nanotubes*, CRC Press, 2017.
76 Y. Seekaew, D. Phokharatkul, A. Wisitsoraat and C. Wongchoosuk, *Appl. Surf. Sci.*, 2017, **404**, 357–363.
77 M.-S. Park, K. H. Kim, M.-J. Kim and Y.-S. Lee, *Colloids Surf., A*, 2016, **490**, 104–109.
78 S. Srivastava, S. K. Jain, G. Gupta, T. Senguttuvan and B. K. Gupta, *RSC Adv.*, 2020, **10**, 1007–1014.
79 X. Gao, Q. Zhou, J. Wang, L. Xu and W. Zeng, *Nanomaterials*, 2020, **10**, 299.
80 J. Ma, M. Zhang, L. Dong, Y. Sun, Y. Su, Z. Xue and Z. Di, *AIP Adv.*, 2019, **9**, 075207.
81 Y. Zhao, J. Zhang, Y. Wang and Z. Chen, *Nanoscale Res. Lett.*, 2020, **15**, 1–8.
82 B. Zhang, G. Liu, M. Cheng, Y. Gao, L. Zhao, S. Li, F. Liu, X. Yan, T. Zhang and P. Sun, *Sens. Actuators, B*, 2018, **261**, 252–263.
83 B. Zhang, M. Cheng, G. Liu, Y. Gao, L. Zhao, S. Li, Y. Wang, F. Liu, X. Liang and T. Zhang, *Sens. Actuators, B*, 2018, **263**, 387–399.
84 S. Tang, W. Chen, H. Zhang, Z. Song, Y. Li and Y. Wang, *Front. Chem.*, 2020, **8**, 174.
85 R. Peng, Y. Li, T. Liu, P. Si, J. Feng, J. Suhr and L. Ci, *Mater. Chem. Phys.*, 2020, **239**, 121961.
86 B. G. Ghule, N. M. Shinde, S. D. Raut, S. F. Shaikh, A. M. Al-Enizi, K. H. Kim and R. S. Mane, *J. Colloid Interface Sci.*, 2021, **589**, 401–410.
87 R. Ghanbari, R. Safaiee, M. H. Sheikhi, M. M. Golshan and Z. K. Horastani, *ACS Appl. Mater. Interfaces*, 2019, **11**, 21795–21806.
88 L. Xue, W. Wang, Y. Guo, G. Liu and P. Wan, *Sens. Actuators, B*, 2017, **244**, 47–53.
89 L. Cai and C. Wang, *Flexible and Stretchable Medical Devices*, 2018, pp. 7–51.
90 N. Ansari, M. Y. Lone, Shumaila, J. Ali, M. Zulfequar, M. Husain, S. Islam and S. Husain, *J. Appl. Phys.*, 2020, **127**, 044902.
91 H. R. Ludwig, S. G. Cairelli and J. J. Whalen, *Documentation for immediately dangerous to life or health concentrations (IDLHS)*, US Department of Health and Human Services, Public Health Service, Centers for Disease Control and Prevention, National Institute for Occupational Safety and Health, Division of Standards Development and Technology Transfer, 1994.
92 I. M. Sharafeldin and N. K. Allam, *New J. Chem.*, 2017, **41**, 14936–14944.
93 S. Kumar, V. Pavelyev, P. Mishra and N. Tripathi, *Bull. Mater. Sci.*, 2020, **43**, 61.
94 T. Han, S. Gao, Z. Wang, T. Fei, S. Liu and T. Zhang, *J. Alloys Compd.*, 2019, **801**, 142–150.
95 Y. R. Choi, Y.-G. Yoon, K. S. Choi, J. H. Kang, Y.-S. Shim, Y. H. Kim, H. J. Chang, J.-H. Lee, C. R. Park, S. Y. Kim and H. W. Jang, *Carbon*, 2015, **91**, 178–187.
96 N. Sharma, R. Vyas, V. Sharma, H. Rahman, S. Sharma and K. Sachdev, *Appl. Nanosci.*, 2020, **10**, 517–528.
97 J. Park, Y. Kim, S. Y. Park, S. J. Sung, H. W. Jang and C. R. Park, *Carbon*, 2020, **159**, 175–184.
98 H. Zhang, J. Feng, T. Fei, S. Liu and T. Zhang, *Sens. Actuators, B*, 2014, **190**, 472–478.
99 P. Cao, Y. Cai, D. Pawar, S. Navale, C. N. Rao, S. Han, W. Xu, M. Fang, X. Liu and Y. Zeng, *Chem. Eng. J.*, 2020, 125491.
100 J. Liu, S. Li, B. Zhang, Y. Wang, Y. Gao, X. Liang, Y. Wang and G. Lu, *J. Colloid Interface Sci.*, 2017, **504**, 206–213.
101 B. Bhangare, N. S. Ramgir, A. Pathak, K. Sinju, A. Debnath, S. Jagtap, N. Suzuki, K. Muthe, C. Terashima and D. Aswal, *Mater. Sci. Semicond. Process.*, 2020, **105**, 104726.
102 Z. Li, Y. Liu, D. Guo, J. Guo and Y. Su, *Sens. Actuators, B*, 2018, **271**, 306–310.
103 Jyoti, N. Kanaujiya and G. D. Varma, *AIP Conf. Proc.*, 2018, **1953**, 030039.

104 R. Purbia, Y. M. Kwon, H.-D. Kim, Y. S. Lee, H. Shin and J. M. Baik, *J. Mater. Chem. A*, 2020, **8**, 11734–11742.
105 B. Liu, X. Liu, Z. Yuan, Y. Jiang, Y. Su, J. Ma and H. Tai, *Sens. Actuators, B*, 2019, **295**, 86–92.
106 E. Dilonardo, M. Penza, M. Alvisi, R. Rossi, G. Cassano, C. Di Franco, F. Palmisano, L. Torsi and N. Cioffi, *Beilstein J. Nanotechnol.*, 2017, **8**, 592–603.
107 C. Hua, Y. Shang, Y. Wang, J. Xu, Y. Zhang, X. Li and A. Cao, *Appl. Surf. Sci.*, 2017, **405**, 405–411.
108 P. B. Agarwal, B. Alam, D. S. Sharma, S. Sharma, S. Mandal and A. Agarwal, *Flexible Printed Electron.*, 2018, **3**, 035001.
109 N. Yi, Z. Cheng, H. Li, L. Yang, J. Zhu, X. Zheng, Y. Chen, Z. Liu, H. Zhu and H. Cheng, *Mater. Today Phys.*, 2020, **15**, 100265.
110 C. Yu, Q. Liu, Z. He, X. Gao, E. Wu, J. Guo, C. Zhou and Z. Feng, *J. Semicond.*, 2020, **41**, 032101.
111 Z. Bo, X. Wei, X. Guo, H. Yang, S. Mao, J. Yan and K. Cen, *Chem. Phys. Lett.*, 2020, 137485.
112 H. S. Hong, N. H. Phuong, N. T. Huong, N. H. Nam and N. T. Hue, *Appl. Surf. Sci.*, 2019, **492**, 449–454.
113 G. Murali, M. Reddeppa, C. Seshendra Reddy, S. Park, T. Chandrakalavathi and M.-D. Kim, *ACS Appl. Mater. Interfaces*, 2020, **12**, 13428–13436.
114 Y.-h. Gui, H.-y. Wang, K. Tian, H.-s. Guo, H.-z. Zhang, S.-m. Fang and Y. Wang, *Ceram. Int.*, 2018, **44**, 4900–4907.
115 F. Niu, Z.-W. Shao, H. Gao, L.-M. Tao and Y. Ding, *Sens. Actuators, B*, 2021, **328**, 129005.
116 Z. Ahmad, S. Manzoor, M. Talib, S. Islam and P. Mishra, *Mater. Sci. Eng., B*, 2020, **255**, 114528.
117 N. Roy, R. Sinha, T. T. Daniel, H. B. Nemade and T. K. Mandal, *IEEE Sens. J.*, 2020, 13245–13252.
118 K. K. Paulla and A. A. Farajian, *J. Phys. Chem. C*, 2013, **117**, 12815–12825.
119 M. Noei, *Vacuum*, 2016, **131**, 194–200.
120 A. Hosseingholipourasl, S. Hafizah Syed Ariffin, M. T. Ahmadi, S. S. Rahimian Koloor, M. Petrů and A. Hamzah, *Sensors*, 2020, **20**, 357.
121 P. Karthik, P. Gowthaman, M. Venkatachalam and A. Rajamanickam, *J. Mater. Sci.: Mater. Electron.*, 2020, **31**, 3695–3705.
122 N. Osouleddini and S. F. Rastegar, *J. Electron Spectrosc. Relat. Phenom.*, 2019, **232**, 105–110.
123 N. Tit, K. Said, N. M. Mahmoud, S. Kouser and Z. H. Yamani, *Appl. Surf. Sci.*, 2017, **394**, 219–230.
124 Z. Zheng and H. Wang, *Chem. Phys. Lett.*, 2019, **721**, 33–37.
125 S. Impeng, A. Junkaew, P. Maitarad, N. Kungwan, D. Zhang, L. Shi and S. Namuangruk, *Appl. Surf. Sci.*, 2019, **473**, 820–827.
126 D. Cortés-Arriagada, N. Villegas-Escobar and D. E. Ortega, *Appl. Surf. Sci.*, 2018, **427**, 227–236.
127 X. Fan, K. Elgammal, A. D. Smith, M. Östling, A. Delin, M. C. Lemme and F. Niklaus, *Carbon*, 2018, **127**, 576–587.
128 E. Salih and A. I. Ayesh, *Phys. E*, 2020, **125**, 114418.
129 F. Özütok, I. K. Er, S. Acar and S. Demiri, *J. Mater. Sci.: Mater. Electron.*, 2019, **30**, 259–265.
130 A. Roy, A. Ray, P. Sadhukhan, K. Naskar, G. Lal, R. Bhar, C. Sinha and S. Das, *Synth. Met.*, 2018, **245**, 182–189.
131 N. John and K. Abraham, *Sens. Actuators, B*, 2020, **325**, 128749.
132 A. Debataraja, N. L. W. Septiani, B. Yuliarto, B. Sunendar and H. Abdullah, *Ionics*, 2019, **25**, 4459–4468.
133 J. H. Butler and S. A. Montzka, *NOAA Earth System Research Laboratory*, 2016, vol. 58.
134 E. Dlugokencky, *NOAA/ESRL*, available at: www.esrl.noaa.gov/gmd/ccgg/trends_ch4/, accessed November, 12, 2018.
135 J. Kathirvelan and R. Vijayaraghavan, *Bull. Mater. Sci.*, 2015, **38**, 909–913.
136 M. T. Humayun, R. Divan, L. Stan, D. Rosenmann, D. Gosztola, L. Gundel, P. A. Solomon and I. Paprotny, *IEEE Sens. J.*, 2016, **16**, 8692–8699.
137 X. Chen, Z. Huang, J. Li, C. Wu, Z. Wang and Y. Cui, *Vacuum*, 2018, **154**, 120–128.
138 C. Wu, J. Li, Z. Guo, T. Zhang, X. Chen and M. Jiao, *J. Electrochem. Soc.*, 2020, **167**, 145501.
139 S. Navazani, M. Hassanisadi, M. Eskandari and Z. Talaei, *Synth. Met.*, 2020, **260**, 116267.
140 S. Nikmanesh, R. Safaiee and M. H. Sheikhi, *Mater. Chem. Phys.*, 2021, **257**, 123808.
141 Z. Wang, T. Zhang, T. Han, T. Fei, S. Liu and G. Lu, *Sens. Actuators, B*, 2018, **266**, 812–822.
142 J. Tawale, A. Kumar, S. Dhakate and A. Srivastava, *Mater. Chem. Phys.*, 2017, **201**, 372–383.
143 G. Chimowa, Z. P. Tshabalala, A. A. Akande, G. Bepete, B. Mwakikunga, S. S. Ray and E. M. Benecha, *Sens. Actuators, B*, 2017, **247**, 11–18.
144 D. Acharyya and P. Bhattacharyya, *IEEE Electron Device Lett.*, 2016, **37**, 656–659.
145 S. Navazani, A. Shokuhfar, M. Hassanisadi, M. Askarieh, A. Di Carlo and A. Agresti, *Talanta*, 2018, **181**, 422–430.
146 H. Roshan, M. H. Sheikhi, M. K. F. Haghighi and P. Padidar, *IEEE Sens. J.*, 2020, **20**, 2526–2532.
147 M. J. Bezdek, S.-X. L. Luo, K. H. Ku and T. M. Swager, *Proc. Natl. Acad. Sci. U. S. A.*, 2021, 118.
148 V. Babrauskas, *J. Fire Sci.*, 2017, **35**, 396–414.
149 D. V. Truong, B. T. Linh, N. M. Kien, L. T. L. Anh, N. C. Tu, N. D. Chien and N. H. Lam, *Mater. Trans.*, 2020, **61**, 1540–1543.
150 V. Le, T. Duong, L. T. Luu, T. Pham, L. Nguyen and T. Nguyen, *J. Met., Mater. Miner.*, 2019, **29**, 61–68.
151 T. Wu, D. Lv, W. Shen, W. Song and R. Tan, *Sens. Actuators, B*, 2020, **316**, 128198.
152 S. Abdulla and B. Pullithadathil, *Langmuir*, 2020, **36**, 11618–11628.
153 N. Ansari, M. Y. Lone, J. Ali, M. Husain and S. Husain, *AIP Conf. Proc.*, 2020, 020033.
154 R. Ridhi, S. Gautam, G. Saini, S. Tripathi, J. Rawat and P. Jha, *Mater. Today: Proc.*, 2020, **28**, 1759–1763.
155 F. Schütt, V. Postica, R. Adelung and O. Lupan, *ACS Appl. Mater. Interfaces*, 2017, **9**, 23107–23118.
156 T. Guo, T. Zhou, Q. Tan, Q. Guo, F. Lu and J. Xiong, *Sensors*, 2018, **18**, 3542.
157 H.-Y. Du, J. Wang, P.-J. Yao, Y.-W. Hao and X.-G. Li, *J. Mater. Sci.*, 2013, **48**, 3597–3604.

158 S. Abdulla, T. L. Mathew and B. Pullithadathil, *Sens. Actuators, B*, 2015, **221**, 1523–1534.
159 J.-H. Lim, N. Phiboolsirichit, S. Mubeen, M. A. Deshusses, A. Mulchandani and N. V. Myung, *Nanotechnology*, 2010, **21**, 075502.
160 D. Zhang, Z. Wu, P. Li, X. Zong, G. Dong and Y. Zhang, *Sens. Actuators, B*, 2018, **258**, 895–905.
161 T. Liang, R. Liu, C. Lei, K. Wang, Z. Li and Y. Li, *Micromachines*, 2020, **11**, 965.
162 M. Jaiswal, R. Kumar, J. Mittal and P. Jha, *Sens. Actuators, B*, 2020, **310**, 127826.
163 V. Haridas, A. Sukhananazerin, J. Mary Sneha, B. Pullithadathil and B. Narayanan, *Appl. Surf. Sci.*, 2020, **517**, 146158.
164 N. Garg, M. Kumar, N. Kumari, A. Deep and A. L. Sharma, *ACS Omega*, 2020, **5**, 27492–27501.
165 X. V. Le, T. L. A. Luu, H. L. Nguyen and C. T. Nguyen, *Vacuum*, 2019, **168**, 108861.
166 S. Saxena and A. K. Srivastava, *AIP Conf. Proc.*, 2020, 020032.
167 O. Hamouma, N. Kaur, D. Oukil, A. Mahajan and M. M. Chehimi, *Synth. Met.*, 2019, **258**, 116223.
168 I. Karaduman, E. Er, H. Çelikkan, N. Erk and S. Acar, *J. Alloys Compd.*, 2017, **722**, 569–578.
169 P. Seifaddini, R. Ghasempour, M. Ramezannezhad and A. Nikfarjam, *Mater. Res. Express*, 2019, **6**, 045054.
170 R. Kumar, A. Kumar, R. Singh, R. Kumar, D. Kumar, S. K. Sharma and M. Kumar, *Mater. Chem. Phys.*, 2020, **240**, 121922.
171 X. Wang, D. Gu, X. Li, S. Lin, S. Zhao, M. N. Rumyantseva and A. M. Gaskov, *Sens. Actuators, B*, 2019, **282**, 290–299.
172 Z. Ye, H. Tai, R. Guo, Z. Yuan, C. Liu, Y. Su, Z. Chen and Y. Jiang, *Appl. Surf. Sci.*, 2017, **419**, 84–90.
173 A. Bisht, S. Chockalingam, O. Panwar, A. Kesarwani, B. Singh and V. Singh, *Sci. Adv. Mater.*, 2015, **7**, 1424–1434.
174 J. Johnson, *Chem. Eng. News*, 2020, **98**(1), 17.
175 S.-Y. Guo, P.-X. Hou, H.-X. Wang, C. Shi, H.-T. Fang and C. Liu, *Carbon*, 2019, **151**, 156–159.
176 J. Park, I. R. Rang, K Lee and H. J. Kim, *Sensors*, 2019, **19**(18), 3878.
177 M. Han, J. K. Kim, J. Lee, H. K. An, J. P. Yun, S.-W. Kang and D. Jung, *J. Nanosci. Nanotechnol.*, 2020, **20**, 4011–4014.
178 J. H. Kim, J. G. Jeon, R. Ovalle-Robles and T. J. Kang, *Int. J. Hydrogen Energy*, 2018, **43**, 6456–6461.
179 C. McConnell, S. N. Kanakaraj, J. Dugre, R. Malik, G. Zhang, M. R. Haase, Y.-Y. Hsieh, Y. Fang, D. Mast and V. Shanov, *ACS Omega*, 2020, **5**, 487–497.
180 M. Xiao, S. Liang, J. Han, D. Zhong, J. Liu, Z. Zhang and L. Peng, *ACS Sens.*, 2018, **3**, 749–756.
181 J. K. Kim, J. Lee, S. H. Kong and D. Jung, *J. Sens. Technol.*, 2018, **27**, 132–136.
182 S. Dhall, K. Sood and R. Nathawat, *Int. J. Hydrogen Energy*, 2017, **42**, 8392–8398.
183 G. Tabares, A. Redondo-Cubero, L. Vazquez, M. Revenga, S. Cortijo-Campos, E. Lorenzo, A. De Andrés, E. Ruiz and J. Pau, *Sens. Actuators, A*, 2020, **304**, 111884.
184 D. Kathiravan, B.-R. Huang and A. Saravanan, *ACS Appl. Mater. Interfaces*, 2017, **9**, 12064–12072.
185 D. Zhang, H. Chang and Y. Zhang, *J. Mater. Sci.: Mater. Electron.*, 2017, **28**, 1667–1673.
186 M. Chen, L. Zou, Z. Zhang, J. Shen, D. Li, Q. Zong, G. Gao, G. Wu, J. Shen and Z. Zhang, *Carbon*, 2018, **130**, 281–287.
187 T. Kamal, *J. Alloys Compd.*, 2017, **729**, 1058–1063.
188 B. Sharma and J.-S. Kim, *Int. J. Hydrogen Energy*, 2018, **43**, 11397–11402.
189 X. Tang, P.-A. Haddad, N. Mager, X. Geng, N. Reckinger, S. Hermans, M. Debliquy and J.-P. Raskin, *Sci. Rep.*, 2019, **9**, 3653.
190 L. S. K. Achary, B. Maji, A. Kumar, S. P. Ghosh, J. P. Kar and P. Dash, *Int. J. Hydrogen Energy*, 2020, **45**, 5073–5085.
191 K. Yan, Y. Toku and Y. Ju, *Int. J. Hydrogen Energy*, 2019, **44**, 6344–6352.
192 M. Han, J. K. Kim, S.-W. Kang and D. Jung, *Appl. Surf. Sci.*, 2019, **481**, 597–603.
193 M. Baro and S. Ramaprabhu, *Int. J. Hydrogen Energy*, 2018, **43**, 16421–16429.
194 Y. Kim, Y. S. Choi, S. Y. Park, T. Kim, S.-P. Hong, T. H. Lee, C. W. Moon, J.-H. Lee, D. Lee and B. H. Hong, *Nanoscale*, 2019, **11**, 2966–2973.
195 X. Lu, X. Song, C. Gu, H. Ren, Y. Sun and J. Huang, *J. Phys. Chem. Solids*, 2018, **116**, 324–330.
196 Q. A. Drmosh, Z. H. Yamani, A. H. Hendi, M. A. Gondal, R. A. Moqbel, T. A. Saleh and M. Y. Khan, *Appl. Surf. Sci.*, 2019, **464**, 616.
197 D. Zhang, N. Yin, C. Jiang and B. Xia, *J. Mater. Sci.: Mater. Electron.*, 2017, **28**, 2763–2768.
198 R. Srivastava, H. Suman, S. Shrivastava and A. Srivastava, *Chem. Phys. Lett.*, 2019, **731**, 136575.
199 S. Bagherzadeh-Nobari, K. H. Istadeh and R. Kalantarinejad, *Phys. E*, 2020, **115**, 113691.
200 I. Ibrahim, A. Khalid and M. A. Wahid, *J. Phys.: Conf. Ser.*, 2018, 1032.
201 E. Salih and A. I. Ayesh, *Mater. Today Commun.*, 2020, 101823.
202 Z. Song, Z. Wei, B. Wang, Z. Luo, S. Xu, W. Zhang, H. Yu, M. Li, Z. Huang and J. Zang, *Chem. Mater.*, 2016, **28**, 1205–1212.
203 Z. Khodadadi, *Phys. E*, 2018, **99**, 261–268.
204 A. Reshak and S. Auluck, *J. Appl. Phys.*, 2014, **116**, 103702.
205 L. Liu, M. Yang, S. Gao, X. Zhang, X. Cheng, Y. Xu, H. Zhao, L. Huo and Z. Major, *ACS Appl. Nano Mater.*, 2019, **2**, 5409–5419.
206 P. S. Shewale and K.-S. Yun, *J. Alloys Compd.*, 2020, 155527.
207 A. Shanmugasundaram, N. D. Chinh, Y.-J. Jeong, T. F. Hou, D.-S. Kim, D. Kim, Y.-B. Kim and D.-W. Lee, *J. Mater. Chem. A*, 2019, **7**, 9263–9278.
208 J. Fan, P. Liu, X. Chen, H. Zhou, S. Fu and W. Wu, *Nanotechnology*, 2019, **30**, 475501.
209 L. Yin, H. Wang, L. Li, H. Li, D. Chen and R. Zhang, *Appl. Surf. Sci.*, 2019, **476**, 107–114.
210 Y. Zhou, Y. Wang and Y. Guo, *Mater. Lett.*, 2019, **254**, 336–339.
211 X. X. Zhang, M. S. Pi, H. Cui, C. D. Chen, Z. G. Zhang and J. Tang, *Front. Chem.*, 2019, **7**, 476.

212 S. Shao, X. Chen, Y. Chen, L. Zhang, H. W. Kim and S. S. Kim, *ACS Appl. Nano Mater.*, 2020, 5220–5230.
213 N. Van Hoang, C. M. Hung, N. D. Hoa, N. Van Duy, I. Park and N. Van Hieu, *Sens. Actuators, B*, 2019, **282**, 876–884.
214 J. Chu, X. Wang, D. Wang, A. Yang, P. Lv, Y. Wu, M. Rong and L. Gao, *Carbon*, 2018, **135**, 95–103.
215 A. Rydosz, *Sensors*, 2018, **18**, 2298.
216 R. Guo, H. Wang, R. Tian, D. Shi, H. Li, Y. Li and H. Liu, *Ceram. Int.*, 2020, **46**, 7065–7073.
217 S. Young and Z. Lin, *Microsyst. Technol.*, 2018, **24**, 55–58.
218 B. Chaitongrat and S. Chaisitsak, *J. Nanomater.*, 2018, 1–11.
219 X. Jia, C. Cheng, S. Yu, J. Yang, Y. Li and H. Song, *Sens. Actuators, B*, 2019, **300**, 127012.
220 N. Kohli, A. Hastir, M. Kumari and R. C. Singh, *Sens. Actuators, A*, 2020, **314**, 112240.
221 M. Yoosefian, H. Raissi and A. Mola, *Sens. Actuators, B*, 2015, **212**, 55–62.
222 X. Zhou, C. Zhao, C. Chen, J. Chen and Y. Li, *Appl. Surf. Sci.*, 2020, 146595.
223 J. Wang, M. Tanaka and M. Okochi, *IEEE Sens. J.*, 2020, 1–3.
224 M. Dai, L. Zhao, H. Gao, P. Sun, F. Liu, S. Zhang, K. Shimanoe, N. Yamazoe and G. Lu, *ACS Appl. Mater. Interfaces*, 2017, **9**, 8919–8928.
225 H. Albaris and G. Karuppasamy, *Appl. Nanosci.*, 2019, **9**, 1719–1729.
226 M. S. B. Reddy, S. Kailasa, B. G. Rani, P. Munindra, K. Bikshalu and K. V. Rao, *SN Appl. Sci.*, 2020, **2**, 1–13.
227 N. L. W. Septiani, B. Yuliarto and H. K. Dipojono, *Appl. Phys. A: Mater. Sci. Process.*, 2017, **123**, 166.
228 Z. Yuan, J. Zhao, F. Meng, W. Qin, Y. Chen, M. Yang, M. Ibrahim and Y. Zhao, *J. Alloys Compd.*, 2019, **793**, 24–30.
229 R. Peng, Y. Li, J. Chen, P. Si, J. Feng, L. Zhang and L. Ci, *Sens. Actuators, A*, 2018, **283**, 128–133.
230 M. Hassan, Z.-H. Wang, W.-R. Huang, M.-Q. Li, J.-W. Liu and J.-F. Chen, *Sensors*, 2017, **17**, 2245.
231 V. Kumar, K. Vikrant and K.-H. Kim, *TrAC, Trends Anal. Chem.*, 2019, **121**, 115694.
232 Z. Bo, M. Yuan, S. Mao, X. Chen, J. Yan and K. Cen, *Sens. Actuators, B*, 2018, **256**, 1011–1020.
233 T. Alizadeh and L. H. Soltani, *J. Hazard. Mater.*, 2013, **248–249**, 401–406.
234 V. Munusami, K. Arutselvan and S. Vadivel, *Diamond Relat. Mater.*, 2020, 108167.
235 R. Peng, Y. Li, T. Liu, P. Si, J. Feng, J. Suhr and L. Ci, *Mater. Chem. Phys.*, 2020, **239**, 121961.
236 Q. Wei, J. Sun, P. Song, J. Li, Z. Yang and Q. Wang, *Sens. Actuators, B*, 2020, **304**, 127306.
237 Y. Seekaew, A. Wisitsoraat, D. Phokharatkul and C. Wongchoosuk, *Sens. Actuators, B*, 2019, **279**, 69–78.
238 D. Wang, L. Tian, H. Li, K. Wan, X. Yu, P. Wang, A. Chen, X. Wang and J. Yang, *ACS Appl. Mater. Interfaces*, 2019, **11**, 12808–12818.
239 M. Taheri, Z. Feizabadi, S. Jafari and N. Mansour, *J. Electron. Mater.*, 2018, **47**, 7232–7239.
240 S. Goutham, N. Jayarambabu, C. Sandeep, K. K. Sadasivuni, D. S. Kumar and K. V. Rao, *Microchim. Acta*, 2019, **186**, 62.
241 L. Zhou, R. Qian, S. Zhuo, Q. Chen, Z. Wen and G. Li, *J. Saudi Chem. Soc.*, 2020, 364–373.
242 Y. Wang, M. Yang, W. Liu, L. Dong, D. Chen and C. Peng, *J. Mater. Chem. C*, 2019, **7**, 9248–9256.
243 S. Dhall, M. Kumar, M. Bhatnagar and B. Mehta, *Int. J. Hydrogen Energy*, 2018, **43**, 17921–17927.
244 M. Morsy, I. Yahia, H. Zahran and M. Ibrahim, *J. Inorg. Organomet. Polym. Mater.*, 2019, **29**, 416–422.
245 F. Cao, C. Li, M. Li, H. Li and B. Yang, *Micro Nano Lett.*, 2018, **13**, 779–783.
246 A. D. K.-T. Lam, Z.-D. Lin, H.-Y. Lu and S.-J. Young, *Microsyst. Technol.*, 2019, 1–4.
247 T. Zhang, S. Mubeen, B. Yoo, N. V. Myung and M. A. Deshusses, *Nanotechnology*, 2009, **20**, 255501.
248 X. Tang, J.-P. Raskin, N. Kryvutsa, S. Hermans, O. Slobodian, A. N. Nazarov and M. Debliquy, *Sens. Actuators, B*, 2020, **305**, 127423.
249 C. Cantalini, L. Valentini, I. Armentano, L. Lozzi, J. M. Kenny and S. Santucci, *Sens. Actuators, B*, 2003, **95**, 195–202.
250 S. Prezioso, F. Perrozzi, L. Giancaterini, C. Cantalini, E. Treossi, V. Palermo, M. Nardone, S. Santucci and L. Ottaviano, *J. Phys. Chem. C*, 2013, **117**, 10683–10690.
251 X. Liu, S. Cheng, H. Liu, S. Hu, D. Zhang and H. Ning, *Sensors*, 2012, **12**, 9635–9665.
252 J. Leclercq and P. Sveshtarov, *Bulg. J. Phys.*, 2016, **43**, 121–147.
253 S. Mao, S. Cui, G. Lu, K. Yu, Z. Wen and J. Chen, *J. Mater. Chem.*, 2012, **22**, 11009–11013.
254 N. Vallabani, S. Mittal, R. K. Shukla, A. K. Pandey, S. R. Dhakate, R. Pasricha and A. Dhawan, *J. Biomed. Nanotechnol.*, 2011, **7**, 106–107.